A Closer Look at the Isomerization of 5-Androstene-3,17-Dione to 4-Androstene-3,17-Dione in Ketosteroid Isomerase

Marek Freindorf, Yunwen Tao and Elfi Kraka*

Computational and Theoretical Chemistry Group (CATCO)
Department of Chemistry, Southern Methodist University
Dallas, TX 75275, USA

*Corresponding author. E-mail: *ekraka@smu.edu*

ABSTRACT: We report a comprehensive investigation of the 5-androstene-3,17-dione to 4-androstene-3,17-dione isomerization in Ketosteroid Isomerase, gas phase and aqueous solution, applying as tools the *Unified Reaction Valley Approach* (URVA) and the *Local Vibrational Mode Analysis*. Conformational changes of the steroid rings are monitored via Cremer-Pople puckering coordinates. URVA identifies simultaneous breakage of the C_α–H bond and O–H bond formation with the catalytic acid, leading to an intermediate with the acid positioned over ring *A* as the major chemical events of the first reaction step. Via a barrier-less shift, a second intermediate is formed with the acid being positioned over ring *B*. Then, according to URVA, breakage of the intermediate O–H bond, the formation of the new C_γ–H bond accompanied by a double bond shift in rings *A* and *B* forms the major chemical events of the second reaction step, which is facilitated by favorable ring puckering. Reactions in protein and gas phase have comparable activation enthalpies, whereas the barrier in aqueous solution is higher, confirming that the major task of the enzyme pocket is to shield the migrating hydrogen atom and the catalyzing acid from interactions with solvent molecules diluting the catalytic power. We do not find exceptional H-bonding with Asp99 and Tyr14, excluding their catalytic activity. There is no strong hydrogen bonding in the TS, which could account for lowering the activation barrier. Our study provides a clear picture of the isomerization process, which will also inspire similar investigations of other important enzymatic reactions.

KEYWORDS: Ketosteroid isomerase; 5-androstene-3,17-dione isomerization; unified reaction valley approach; local mode analysis; ring puckering coordinates; DFT; QM/MM.

1. INTRODUCTION

Ketosteroid Isomerase (KSI) is one of the most efficient enzymes catalyzing chemical reaction with reaction rates approaching the diffusion limit for biologically relevant systems,[1–3] and therefore, has attracted a lot of attention in the field during the past decades.[4–9] One intriguing example is KSI *Commamonas testosteroni*. KSI is a small dimeric enzyme consisting of 125 amino acid residues per monomer (Mr = 13.5 kDa), involved in steroid biosynthesis and transformation of an inactive cholesterol to the hormonally active ketosteroids[10] such as the catalysis of a wide variety of reactions transforming 3-oxo-Δ^5 ketosteroids into their corresponding Δ^4-conjugated isomers.[11,12] These typical two-step reactions involve C–H activation (i.e., C–H breakage/formation), generally an energy demanding

process, followed by double-bond isomerization[13] which is effectively supported by a deprotonated aspartic acid being located in the active site of the enzyme, bringing the energy barrier down in to the 6–10 kcal/mol range making it possible at body-temperature.[11,14–16]

Talalay and Wang showed already in 1955 in their landmark paper[17] that in contrast to acid- and base-catalyzed transformations of conjugated keto-olefins (from β, γ- to the α, β- carbon position) as found in organic chemistry, the enzymatic activity of KSI is

distinct from related non-enzymatic isomerizations as the hydrogen atoms of the steroid substrate are not substantially exchanged with those of a buffered aqueous solution. This implies that the putative active site base in KSI is sufficiently shielded from bulk water to conserve the migrating hydrogen at the 4-position (i.e., α-carbon) and move it directly to the 6-position (γ-carbon) of the steroid. These findings formed the basis for a series of subsequent mechanistic investigations and discussions.

There is still an ongoing debate among experimentalists and theoreticians regarding the role of hydrogen bonds and electrostatic interactions as well as their interplay leading to the observed and calculated small energy barriers in the range of only 6–8 kcal/mol. One of the studies of KSI's exceptional catalytic activity suggested hydrogen bonding between Tyr14 and the substrate carbonyl oxygen as a key player[12] based on NMR experiments.[18] Another explanation involves the formation of low-barrier hydrogen bonds (LBHBs) involving Tyr14, Asp99 and the substrate carbonyl oxygen,[4,19] also supported by NMR experiments. The role of hydrogen bond networks in KSI was further investigated computationally[1,20] showing how these networks can give rise to large local electric fields in the enzyme.[6,7] Multiple hydrogen bond interactions with individually modest contributions adding up to the catalytic strategy for KSI were discussed based on molecular dynamics (MD) simulations and quantum chemical (QM) calculations.[21] Stabilization of the transition states (TSs) and the potential intermediate in KSI reactions were studied computationally.[22] LBHB and the cooperative hydrogen-bond mechanisms were further investigated at the QM level of theory,[23] showing that both mechanisms are equally stabilizing. The role of short-strong hydrogen bonds (SSHBs) in the enzyme was analyzed using the UV spectroscopy.[24] Electronic inductive effects along the hydrogen bond networks were investigated with hybrid QM/MM methodologies.[25] Constrained hydrogen bonding in KSI was studied using high resolution X-ray crystallography, NMR spectroscopy, and QM calculations, showing how packing and binding interactions within the KSI active site are responsible for the enzyme activity.[2,26] The effect of hydrophobic environments and compact packing in the KSI catalytic site was also investigated by site-directed mutagenesis of the enzyme.[27] Using NMR, high-resolution X-ray crystallography, and QM/MM computational method, the structural coupling throughout the active site hydrogen bond networks was investigated for two variants of KSI and compared with the active site of yellow protein,[28]

and the proton delocalization in the H-bonding network of KSI was analyzed using UV and NMR spectroscopy.[29]

Electrostatic interactions in the KSI active site were analyzed theoretically and conceptually, revealing the crucial role of electrostatic preorganization for KSI catalytic activities.[5,30,31] The contribution of electrostatic interactions to the enzyme activity was also investigated by variety of computational studies[9,20,32–40] as well as by experiments using vibrational Stark effect spectroscopy.[38,41–43] Using Tyr14 mutations in KSI, it has been shown that the electrostatic environment of Ox does not provide a great enhancement of the KSI activity.[44] The rigid water dipoles at the active site of KSI were studied with time-resolved vibrational spectroscopy showing that the electrostatic environment plays a key feature for efficient catalysis.[45,46] The heterogeneous and anisotropic origins of the electrostatic environment within the KSI active site were investigated from multiple positions and orientations by using X-ray crystallography, vibrational, UV, and NMR spectroscopy.[47,48] On the other hand, using time-resolved fluorescence spectroscopy significantly changes the electrostatic environment in the active site of KSI taking place during the catalytic reactions could be rolled out.[49] A recent statistical analysis of ca. 45 new crystal structures of KSI-substrate complexes has suggested that also conformational changes of the steroid substrate rings could facilitate KSI's activity[2,50] adding another component.

The overall conclusion of these diverse investigations has been that the strong, unique catalytic activity of KSI is most likely a result of different smaller well-synchronized contributions adding up rather than being based more or less on one dominant source.[1,51] However, more specific details about the possible source(s) of the catalytic power of KSI are needed to derive a more complete picture and to understand the catalytic mechanism in a more holistic way.

We investigated in this work the two-step isomerization of 5-androstene-3,17-dione to 4-androstene-3,17-dione in wild type (WT) KSI (reaction R1), which has served as a prototypic example in numerous experimental and theoretical studies.[12,16,37,52] From a biological point of view, in mammals this reaction constitutes an essential step in the biosynthesis of steroid hormones which have a facet of different biological implications, such as the transformation of cholesterol to testosterone.[10,16,52]

To further elucidate the catalytic effect of Asp38 in the protein and to test the postulated shielding of the enzyme active site pocket conserving the migrating
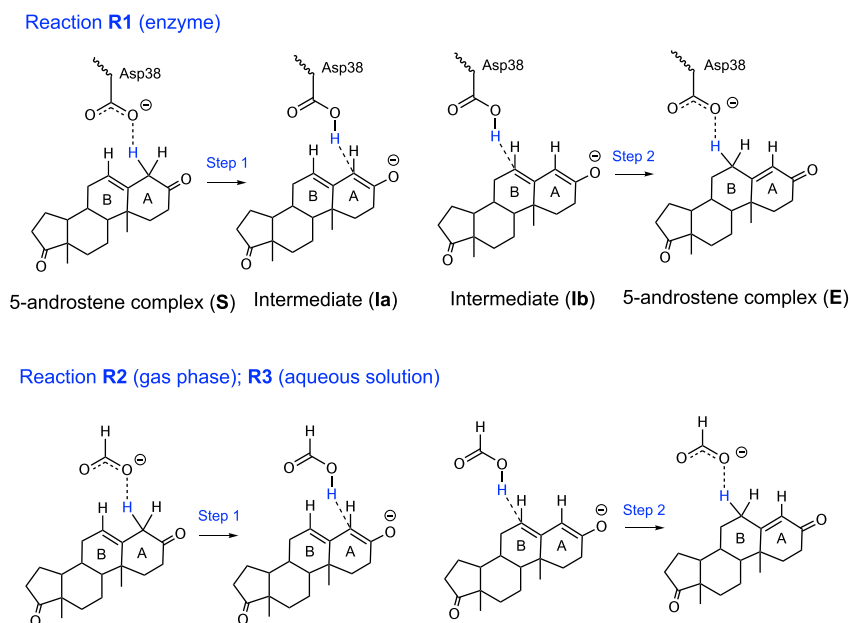
Fig. 1. (Color online) Two-step isomerization of 5-androstene-3,17-dione to 4-androstene-3,17-dione investigated in this work; R1: Reaction in KSI, R2: Gas-phase reaction with Asp38 simulated by formic acid, R3: Reaction in aqueous solution.

hydrogen from interactions with surrounding bulk water, we also modeled the reaction in the gas phase, reaction R2 and in aqueous solution reaction R3, simulating Asp38 with formic acid, as shown in Fig. 1. The pK_a values of formic acid ($pK_a = 3.74$)[53] and that of the aspartic acid side-chain ($pK_a = 3.90$)[54] are comparable. The major goal of this study was to shed new light into the overall catalytic function of KSI targeting in particular the following questions still under debate as described above: (i) what is the role of the enzyme environment, such as electrostatic field effects including charge transfer and space confinement; (ii) does ring-puckering of the substrate play any noticeable role; (iii) does the activation energy benefit from TS stabilization, such as strong hydrogen bonding; (iv) what is the role of Tyr14 and Asp99 in stabilizing the postulated oxoanion hole, in reactant and product, TSs and the intermediates. As special tools for our investigation we utilized the *Unified Reaction Valley approach* (URVA) and the *Local Mode Analysis*, (LMA) which is briefly described in the following.

A comprehensive review of the URVA methodology can be found in Ref. 55, the theoretical basis and background of URVA have also been thoroughly described in Refs. 56–58. Selected URVA applications including enzyme studies are discussed in Refs. 57, 59–68. URVA requires a representative reaction path which is followed by the reaction complex (RC), i.e., the union of reacting molecules on its way from the entrance channel, via the TS to the exit channel on the potential energy surface (PES) of the reaction. As the reaction proceeds, the electronic structure of the RC changes, which is registered by vibrational modes perpendicular to the long amplitude motion along the reaction path spanning the so-called *Reaction Valley*. As described in the seminal Miller, Handy, and Adams paper on the *Reaction Path Hamiltonian*, these vibrational modes couple with the translational motion along the reaction path and the sum of all coupling elements defines the scalar reaction path curvature.[69] Hence, any chemical change is reflected by changes in the scalar reaction path curvature.

We further decompose the scalar reaction path curvature into components, e.g., internal coordinates representing bond lengths, bond angles, and dihedral angles, as well as puckering coordinates or pyramidalization angles,[56] which allows to assign the reaction path curvature maxima to specific events occurring along the reaction path, such as bond formation/cleavage processes, atomic rehybridization conformational changes and so on, providing a detailed insight into the reaction mechanism. In contrast to the reaction path curvature peaks, the curvature minima correspond to minimal electronic structure changes of the reaction complex, often reflecting the beginning of a new chemical event. In this way curvature minima and maxima can be used to divide the entire reaction path into chemically meaningful reaction phases[67,68]

providing a close look at what happens at certain locations on the reaction path. It has to be noted that only chemical events occurring before the TS contribute to the energy barrier, so that the careful analysis of the curvature peaks in the entrance provides, e.g., helpful hints on how to lower a barrier.[55] The curvature profiles were complemented by an analysis of the changes of atomic and molecular charges along the reaction path based on the natural bond orbital (NBO) analysis,[70,71] as well as the analysis of conformational changes of the six-membered carbon rings involved in the isomerization using Cremer–Pople puckering coordinates.[72,73]

The strength of individual bonds of all stationary points on the PES, i.e., reactants, TSs, and products was determined with LMA, which is based on vibrational spectroscopy. The theoretical background of LMA, originally developed by Konkoli and Cremer[74–78] can be found in a comprehensive review paper.[79] The local vibrational modes of a molecule can be considered as the local counterparts of normal vibrational modes, which are generally delocalized due to electronic and mass-coupling.[80] Therefore associated normal mode stretching force constants are of limited use as individual bond strength descriptors. In contrast, local vibrational stretching force constants derived from uncoupled local vibrational modes directly reflect the intrinsic strength of a chemical bond and/or weak chemical interaction.[81] We have successfully applied local stretching force constants to characterize covalent bonds[82–88] and weak chemical interactions such as halogen bonds,[89–94] chalcogen bonds,[95–97] pnicogen bonds,[98–100] tetrel bonds,[101] and hydrogen bonds,[102–110] as well as so-called πhole interactions.[111] LMA was further complemented with the topological analysis of the electron density using Bader's quantum theory of atoms–in–molecule (QTAIM).[112–115]

2. COMPUTATIONAL METHODS

We used in this study as reaction path the intrinsic reaction coordinate (IRC) path of Fukui.[116] All IRC calculations presented in our study were performed with the improved reaction path following procedure of Hratchian–Kraka,[117] which allows to accurately trace the reaction path and its curvature far out into entrance and exit channel and leads to reliable vibrational frequencies along the IRC which are needed to span the reaction valley. Calculations were performed with a B3LYP/6–31G(d,p) model chemistry, i.e., the B3LYP density functional[118–121] and Pople's 6–31G(d,p) basis set[122,123] using an ultrafine grid and tight convergence

criterion with a step size of $s = 0.03$ amu$^{1/2}$ Bohr. For reaction R3 we utilize the polarizable continuum solvent model (PCM) of Tomasi and co-workers[124,125] to simulate the aqueous solution environment. (A comparison of the energetics of reactions R2 and R3 with 6–31G(d,p) and 6–311G(d,p) basis sets is shown in Table S1, Supporting Materials.)

For the reaction R1 we started from a crystal structure of D38N mutant enzyme [PDB: 1OHP, chain A],[126] where residue 38 was changed back to deprotonated aspartic acid. The steroid molecule was placed in the active site of the enzyme with a geometry resembling the TS geometry obtained in the gas-phase calculations of the reaction R2. Then we performed an energy minimization of the entire protein with AMBER,[127] where hydrogen atoms were placed according to standard rules of the AMBER force field. In the AMBER energy minimization the steroid molecule was frozen at its TS geometry of the gas phase. The final protein structure was divided into a QM part which includes the steroid molecule and the COO-side chain of Asp38, and a MM part involving the rest of the protein. A hydrogen link atom was placed on the COO-side chain of Asp38 in order to cap the QM subsystem. The QM/MM TS optimization followed by the IRC calculations were performed with the ONIOM method[128] and the B3LYP/6–31G(d,p)/AMBER level of theory was applied with the ultrafine grid and the IRC step size of $s = 0.05$ amu$^{1/2}$ Bohr.

The analysis of the stationary points was performed at the endpoints of the IRCs and the corresponding transitions states. Particularly, for the enzyme reaction, this is important because the energies of stationary points calculated with QM/MM cannot directly be compared. QM/MM calculations imply simultaneous geometry optimizations of the QM and MM parts. Changes in the QM part during the geometry optimization e.g., of reactant or product complex can induce different changes in the corresponding MM part leading to different local minima of the protein with a different total energy. In the QM/MM IRC calculations done with a small step on the reaction coordinate, the changes of the QM part are done gradually which prevents moving the protein structure into a different local minimum. For easier comparison, the local mode stretching force constants k^a can be transformed into dimensionless bond strength orders (BSO) via a power relationship based on a generalized Badger rule[67,83]: $BSO = A * (k^a)^B$, where the constants A and B are determined by two reference molecules with known BSO and k^a values, and a zero value of the force constant for a zero value of BSO. As reference molecules,

we have used CH_4 as a molecule representing a C–H bond of a BSO value of 1.0, H_2O as a molecule representing an O–H bond of a BSO value of 1.0, and F_2H^- anion (with a 3-center 4-electron structure) as a molecule representing a chemical bond with a hydrogen atom having a BSO value of 0.5, which was used for both the C–H and O–H chemical bonds in our study. For the C–H bond the A and B values are 0.4593 and 0.4633, respectively, and for the O–H bond these values are 0.4680 and 0.3606. The covalent character of a chemical bond/weak chemical interaction can be obtained using the Cremer–Kraka criterion,[129,130] which is based on the value of the energy density H_ρ taken at the bond critical point $\mathbf{r}_\rho$ between the two atoms involved in the chemical bond or weak chemical interaction. A negative value of H_ρ indicates the co-valent character of the bond/interaction whereas a positive value reflects dominant electrostatic character.

All DFT calculations were performed with Gaussian09.[131] The URVA analysis was carried out with the program pURVA.[132] The puckering analysis was performed with the program RING[133] and the local mode analysis with program LModeA.[134] Natural bond orbital (NBO) charges were calculated with the program NBO6[135] and the energy density at bond critical points was obtained with the AIMALL program.[136]

3. RESULTS AND DISCUSSION

Energetics. Both the enzyme reaction R1 as well as the reaction in the gas-phase R2 and in aqueous solution R3 follow a two-step mechanism with an intermediate van der Waals complex (see Figs. 1 and S1, Supporting Materials). As reflected by the data in Table 1, activation enthalpies for Step 1 range from 6.6 kcal/mol to

11.4 kcal/mol, whereas Step 2 reactions proceed with an almost negligible barrier, $H^a = 0.4$ kcal/mol for reaction R1, or in the case of reactions R2 and R3 without any barrier. Calculated activation enthalpies for reaction R1 are in good agreement with the experimental values derived from the D38E mutation of wild type KSI[137] (6.6 kcal/mol versus 7.6 kcal/mol for Step 1 and 7.7 kcal/mol versus 9.2 kcal/mol for Step 2, respectively) confirming the quality of our calculations. It is noteworthy that the activation enthalpies of Step 1 in the enzyme and in the gas phase are very similar (6.6 kcal/mol, R1 versus 6.1 kcal/mol, R2, respectively) confirming Talalay's hypothesis that the enzyme pocket shields the migrating hydrogen atom. This is also fully in line with our observation that in the aqueous solution allowing solvent solute interaction the activation barriers increases considerably (6.1 kcal/mol, R2 versus 11.4 kcal/mol, R3, respectively).

All Step 1 reactions are endothermic with a H_R of 7.3 kcal/mol value for reaction R1 which is comparable to that of the gas-phase reaction R2, confirming again that the gas-phase situation perfectly models the shielding of the migrating proton. In the aqueous solution reaction R3, which allows the interaction between the migrating H-atom and the solvent, the H_R value increases to 13.1 kcal/mol. In contrast to Step 1, Step 2 reactions are strongly exothermic with H_R values ranging between -16 kcal/mol and -20 kcal/mol. These data suggest that once the intermediate is formed, the final isomerization to 4-androstene-3,17-dione, which benefits from double bond delocalization, is straightforward. It has to be noted that the IRC endpoint of the product channel of Step 1, i.e., intermediate **Ia** has a slightly different energy than the IRC endpoint of the entrance channel of Step 2, **Ib**,

Table 1. Energetics of the 5-androstene-3,17-dione isomerization reaction.

Reaction	Step 1		Step 2		Step 1		Step 2	
	E^a	E_R	E^a	E_R	H^a	H_R	H^a	H_R
R1	10.5	8.5	11.1(2.6)	$-9.4(-17.9)$	6.6	7.3	7.7(0.4)	$-8.5(-15.8)$
R2	9.6	9.0	—[a]	$-12.7(-26.1)$	6.1	7.7	—[a]	$-12.2(-19.9)$
R3	15.0	14.2	—[a]	$-6.3(-20.5)$	11.4	13.1	—[a]	$-6.1(-19.2)$
Exp[b]					7.6		9.2	

Notes: [a]Barrier-less reaction.
[b]H^a derived from the D38E protein mutation.[137]
E^a: activation energy, E_R: reaction energy, H^a: activation enthalpy, H_R: reaction enthalpy, all values in (kcal/mol). R1: Isomerization catalyzed by KSI, B3LYP/6–31G(d,p)/AMBER. R2: Gas-phase isomerization catalyzed by formic acid, B3LYP/6–31G(d,p). R3: Isomerization in aqueous solution, B3LYP/6–31G(d,p)/PCM. Values for Step 2 are given relative to the reactants **S** of Step 1, values relative to the intermediates **Ib** are given in parenthesis.
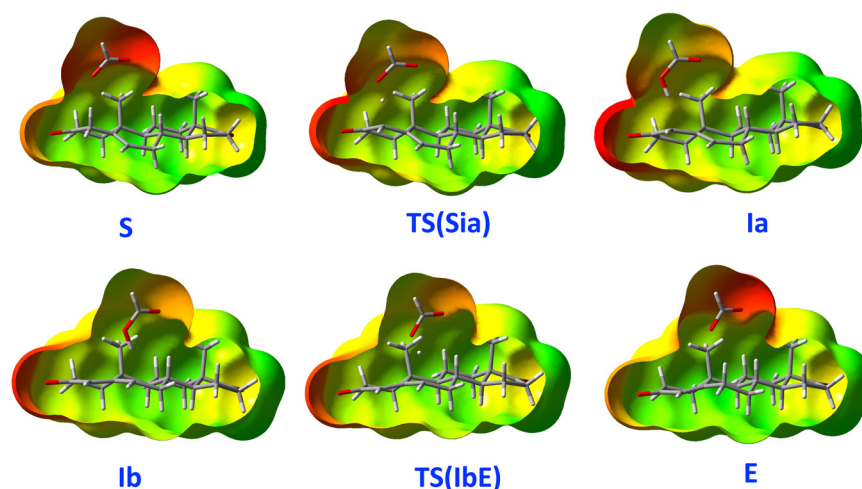
Fig. 2. (Color online) Electrostatic potential mapped on the electronic density calculated at all stationary points of Steps 1 and 2 for the enzyme isomerization R1.

ca. 1 kcal/mol. The difference results from the different positions of the migrating H-atom and the Asp38/formic acid relative to the steroid (see Fig. 1). In **Ia** the migrating H atom and as well as the catalyzing acid are located above ring A of the steroid, whereas in **Ib** they are located above ring B, as visualized in the electrostatic potential maps shown in Fig. 2.

In summary, the energetics show important overall trends, however they do not provide us with mechanistic details and are not able to answer questions such as (i) how do different chemical events such as bond formation/breaking, rehybridization and conformational changes contribute to the activation barrier and (ii) although in both steps C–H bonds are broken, C and O atoms are rehybridized, why is the second step obviously much more effortless than the first step? These questions are targeted in the following.

Reaction mechanism. As depicted in Fig. 1, Step 1 is characterized by a proton transfer from the C4-atom (α-carbon) of the substrate to the side chain of the deprotonated Asp38 residue forming an intermediate dienolate. In Step 2, the proton transfers back from the Asp38 residue to the allylic C6 atom (γ-carbon) of the substrate involving a double bond shift from ring B to ring A.

Figures 3(a) and 3(b) show the energy and curvature profiles for the first step of the isomerization reaction R1 in KSI. According to Fig. 3(b) the reaction can be divided into five distinct phases. Preparation phases 1 and 2 with small curvature enhancements $K1$ and $K2$ are characterized by the approach and orientation of Asp38 and the ketosteroid, which stretch over more than 14 s units (dashed decomposition line in Fig. 3(b),

calculated from the sum of internal components describing the position of Asp38 relative to the steroid substrate). Then two relatively short chemical phases 3 and 4 with two large curvature peaks $K3$ and $K4$ follow where the C_α–H bond is cleaved and the new O–H bond with Asp38 is formed. In phase 5, with curvature peak $K5$, the intermediate dienolate adapts is final conformation, as denoted by the dashed component in Fig. 3(b). In phase 3 the C_α–H bond starts to break (supportive, component with positive sign) while at the same time the formation of the new O–H bond is still resisting (component with negative sign). After the TS in phase 4 bond breaking/formation is finalized. O–H and C–H bonds change roles; the O–H bond component becomes supportive and the C_α–H contribution resistant. Figure 3(a) and Table 2 show the energy contribution of each reaction phase to the reaction barrier. Phases 1 and 2 contribute with 4.1 kcal/mol (40%) to a substantial part of the activation energy compared with the start of C–H bond cleavage and O–H bond formation (phase 3: 5.9 kcal/mol, phase 4: 0.5 kcal/mol). It has to be noted that all chemical events occurring after the TS do not contribute to the activation energy, including the finalization of O–H bond formation and C–H bond breaking (phase 4) and the conformational adjustments of the intermediate dienolate (phase 5).

According to Fig. 3(d), C_a–H bond cleavage and formation of the intermediate O–H bond with the acid proceed in the gas phase with the same mechanism as in the enzyme, i.e., starting with conformational adjustments in phases 1 and 2 making up 4.1 kcal/mol of the activation energy (44%) followed by the start of
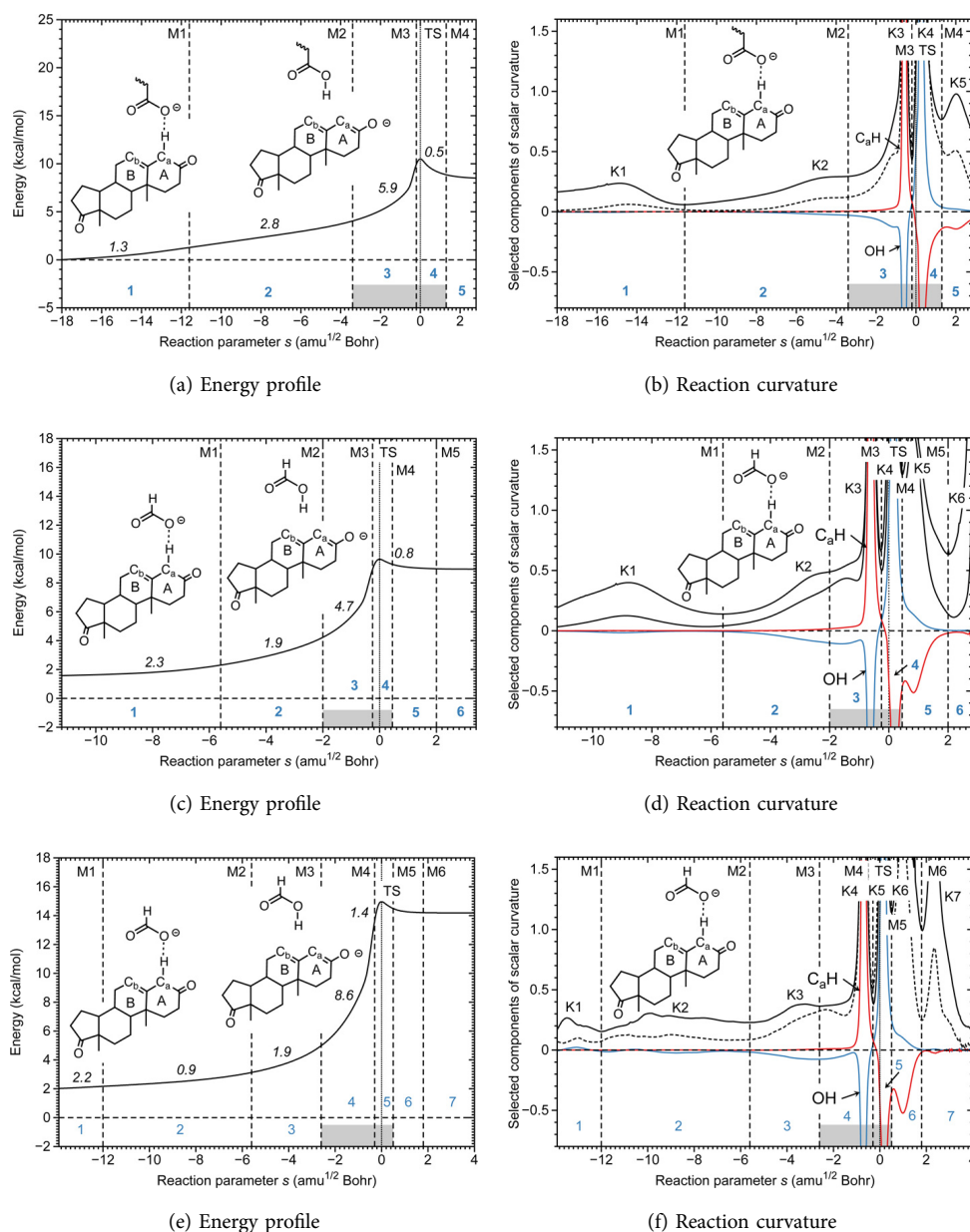
(a) Energy profile

(b) Reaction curvature

(c) Energy profile

(d) Reaction curvature

(e) Energy profile

(f) Reaction curvature

Fig. 3. (Color online) (a) Energy and (b) reaction path curvature profiles for Step 1 of reaction R1 in KSI; (c) Energy and (d) reaction path curvature profiles for Step 1 of reaction R2 in the gas phase; (e) Energy and (f) reaction path curvature profiles for Step 1 of reaction R3 in aqueous solution. The borders of the reaction phases are indicated by vertical dashed lines at curvature minimums $M1$, $M2$, $M3$, etc. and the curvature maximums are indicated by $K1$, $K2$, $K3$, etc. The reaction phases are indicated by the blue numbers. The TS at $s = 0$ amu$^{1/2}$ Bohr is also indicated by a vertical dotted line. The dashed decomposition line represents the orientation of acid and steroid, see text. The gray bar indicates the chemical phase.

C_a–H bond cleavage and O–H bond formation (5.5 kcal/mol), see Fig. 3(c) and Table 2. The overall mechanism remains the same in aqueous solution, as revealed by Fig. 3(f), the major difference is that C_a–H bond cleavage is more difficult; whereas the contribution of the pre-chemical phases to the activation energy is slightly reduced compared to the enzyme reaction (33% versus 40%), the contribution of phases 3 and 4, the barrier is increased (67%), see Fig. 3(e) and Table 2.

These findings clearly confirm Talalay's hypothesis that the enzyme pocket conserves the migrating hydrogen from interactions with surrounding bulk water "diluting" its attraction of the catalyzing acid, underlined by the similarity of enzyme and gas phase results, which shows that this is the major role of the enzyme in the catalytic process rather than special electrostatic field effects, as also ruled out by time-resolved fluorescence spectroscopy studies.[49]

Table 2. Energy contribution (En) of each reaction phase (Ph) to the reaction barrier for the reactions R1–R3. All values in kcal/mol.

	R1			R2			R3	
Ph	En[a]	En[b]	Ph	En[a]	En[b]	Ph	En[a]	En[b]
Step 1								
1	1.3	1.3	1	2.3	2.3	1	2.2	2.2
2	2.8	4.1	2	1.9	4.2	2	0.9	3.1
3	5.9	10.0	3	4.7	8.9	3	1.9	5.0
4	0.5	10.5[c]	4	0.8	9.6[c]	4	8.6	13.6
						5	1.4	15.0[c]
Step 2								
1	0.4	0.4						
2	2.3	2.6[c]						

Notes: [a]Energy contribution of the reaction phase.
[b]Energy at the end of the reaction phase.
[c]Energy up to TS contained in this phase.

Figure 4 shows the energy and reaction path curvature profiles of the second step of the isomerization in the enzyme, which, starting from the intermediate dienolate anion, proceeds with a small energy barrier of only 2.6 kcal/mol, as shown in Table 1. As depicted by Fig. 4(b), the barrier is made up from minor conformational rearrangements leading to small curvature enhancement $K1$ in phase 2 and the actual O–H bond breaking and C_γ–H bond forming processes (peaks $K2$ and $K3$) occur in the exit channel, after the TS, and in this way they no longer contribute to the energy barrier. In summary, the curvature profile provides a clear rational for the energetics.

Ring conformation. In the following, the suggested influence of conformational changes of the steroid substrate rings A and B on KSI's activity[2,50] is

investigated. During the isomerization process the α-carbon of ring A changes from its sp^3 hybridization in 5-androstene-3,17-dione to sp^2 hybridization in 4-androstene-3,17-dione whereas the γ-carbon of ring B changes from sp^2 to sp^3 hybridization. The accompanying double bond shifts lead to conformational changes in both rings.

Figure 5(a) decomposes the reaction path curvature into pyramidalization angle contributions for the six carbon atoms of ring A for Step 1 of reaction R1, Fig. 5(b) decomposes the reaction path curvature into pyramidalization angle contributions for the six carbon atoms of ring B for Step 2 of reaction R1, visualizing in this way the rehybridization process. In both the steps, rehybridization as reflected by the pyramidalization angles contributes to the chemical phases, i.e., phases 3 and 4, curvature peaks $K3$ and $K4$ in Step 1 and curvature peaks $K2$ and $K3$ in Step 2. The same features were found for the gas phase and aqueous solution reactions (the corresponding curvature plots for reaction R2 are shown in Fig. S2, Supporting Materials), amplifying that the overall mechanism is the same in all three media.

In addition, we performed in this work a comprehensive ring puckering analysis based on the Cremer–Pople puckering coordinates.[72,73] Using puckering coordinates, the full set of $3N-6$ independent Cartesian coordinates of any puckered N-membered ring can be uniquely determined via $N-3$ puckering coordinates (amplitude q and puckering angle Φ), $N-3$ bond angles and N bond lengths.[72,73] Six-membered rings can adapt three basis conformations, chair, boat or Twist-boat as well conformations being composed of a particular percentage of these basic
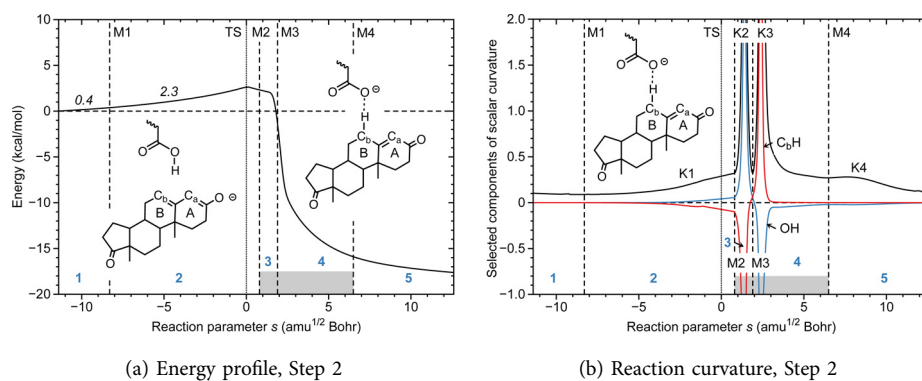

(a) Energy profile, Step 2

(b) Reaction curvature, Step 2

Fig. 4. (Color online) The energy profile (a) and the reaction curvature (b) of the reaction R1 Step 2. The borders of the reaction phases are indicated by vertical dashed lines at curvature minimums $M1$, $M2$, $M3$, etc. and the curvature maximums are indicated by $K1$, $K2$, $K3$, etc. The reaction phases are indicated by the blue numbers. The TS at $s = 0$ amu$^{1/2}$ Bohr is also indicated by a vertical dotted line. The gray bar indicates the chemical phase.

(a) Ring A carbon atoms in Step 1   (b) Ring B carbon atoms in Step 2

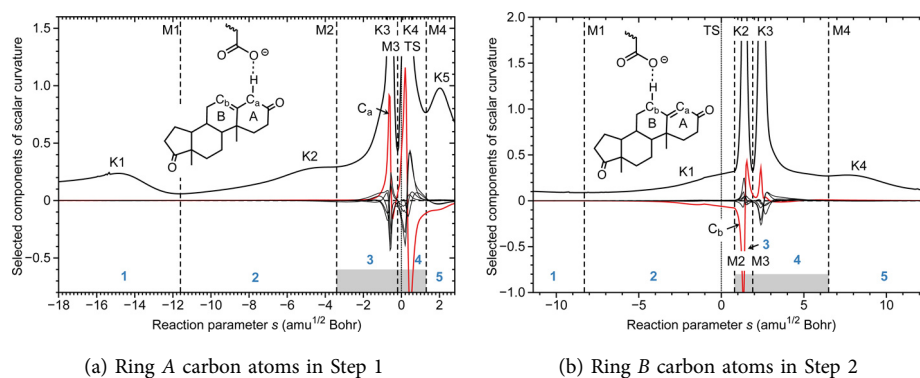**Fig. 5.** (Color online) (a) Decomposition of the reaction path curvature into pyramidalization angle contributions for the six carbon atoms of ring A for Step 1 of reaction R1 the α-carbon contribution is shown in red; (b) Decomposition of the reaction path curvature into pyramidalization angle contributions for the six carbon atoms of ring B for Step 2 of reaction R1 the γ-carbon contribution is shown in red. The borders of the reaction phases are indicated by vertical dashed lines at curvature minimums $M1$, $M2$, $M3$, etc. and the curvature maximums are indicated by $K1$, $K2$, $K3$, etc. The reaction phases are indicated by the blue numbers. The TS at $s = 0$ amu$^{1/2}$ Bohr is also indicated by a vertical dotted line. The gray bar indicates the chemical phase.

forms and their ring puckering can be described by two puckering amplitudes q_2 and q_3, a pseudo-rotation phase angle Φ_2, a hyperspherical angle Θ and total puckering amplitude Q.[138,139] These parameters can be expressed in terms of $6 - 3 = 3$ puckering coordinates, the pseudo-rotational coordinate pair (q_2, Φ_2) describing the pseudo-rotation of boat and twistboat forms, and the crown puckering amplitude q_3, which describes the chair conformer,[72,140] which lead the percentage of the chair, boat, and Twist-boat forms according to the following formulas[72]:

$$\text{Chair} : 100\% \frac{q_3{}^2}{Q^2}, \qquad (1)$$

$$\text{Boat} : 100\% \frac{q_2{}^2}{Q^2} \cos^2(3\Phi_2), \qquad (2)$$

$$\text{TwistBoat} : 100\%[1 - \cos^2(3\Phi_2)] \frac{q_2{}^2}{Q^2}. \qquad (3)$$

In Table 3, the chair, boot, and Twist-boat compositions of the steroid rings A and B, evaluated at all stationary points utilizing Eqs. (1)–(3), are summarized. Noteworthy are the different puckering patterns of **Ia** and **Ib** reflecting the different location of the migrating H atom, being closer to the α-carbon in **Ia** and closer to the γ-carbon in **Ib**. In the reactants **S** of Step 1, i.e., the 5-androstene-3,17-dione, the α-carbon of ring A is sp^3 hybridized. Consequently, ring A has a predominant chair conformation with 78.5%, 99.0%, and 99.2% for reactions R1, R2, and R3, respectively. The value for the enzyme is somewhat smaller, caused by the space confinement in the enzyme pocket. On the other hand, in products **E** of Step 2, i.e., the 4-androstene-3,17-dione, the γ-carbon of ring B is sp^3

hybridized and has a predominant chair conformation with 90.1%, 97.3%, and 97.7% for reactions R1, R2, and R3, respectively. Obviously, ring B has more flexibility to adjust to the chair form than ring A. The γ-carbon of ring B in reactant **S** and the α-carbon of product **E** in ring A are sp^2 hybridized. Both cyclohexene and cyclohexenone rings are known to prefer a half-chair form,[138] which is reflected by an almost equal admixture of chair, boat and Twist-boat conformations found for **E**, see Table 3. Intermediate **Ib** has a relatively large chair contribution (78.3%, 82.6%, and 63.9% for reactions R1, R2, and R3, respectively). This indicates that the γ-carbon of Ring B has already a dominant sp^3 hybridization, facilitating the proton transfer and in this way lowering the activation energy of Step 2.

A more detailed insight into how ring puckering puckering changes during the isomerization reaction can be gained by the decomposition of the reaction path curvature into puckering coordinates. Figure 6 shows the decomposition of the reaction path curvature into puckering amplitudes q_2, q_3 and puckering angle Φ_2 of rings A and B for Steps 1 and 2 of the enzyme reaction R1. The corresponding plots for reactions R2 and R3 are shown in Fig. S3, Supporting Materials. In both steps, puckering contributes to the reaction path curvature in the chemical phases 3 and 4. However, there is an important difference. In Step 1, peak $K3$ is characterized by large supporting $q_2(A)$ component, a strongly resisting $q_3(A)$ component (reflecting changes in the chair conformation of ring A), and smaller resisting $q_2(B)$ and $\Phi_2(B)$ components, which all contribute to the energy barrier. For Step 2, supportive $q_3(B)$ and $q_2(B)$ are most characteristic, reflecting that
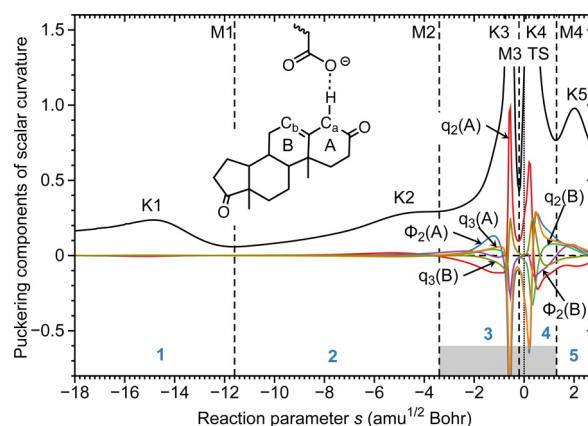
Table 3. Chair, boat and Twist-boat puckering conformers (%) of rings A and B for the reactions R1–R3 evaluated at the stationary point, i.e., IRC endpoints and TSs of Step 1 and Step 2, respectively.[a]

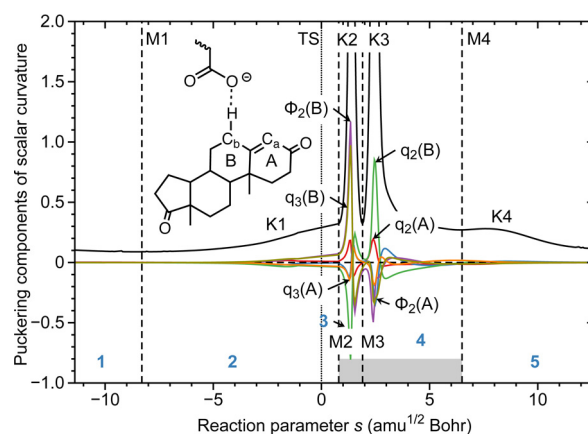|	Step 1			Step 2		
Ring	Chair	Boat	Tboat	Chair	Boat	Tboat
			Reaction R1			
Ring A						
Re	78.5	17.6	4.0	37.1	28.5	34.4
TS	72.9	21.1	6.0	35.7	28.2	36.1
Pr	59.7	16.3	24.0	27.5	53.2	19.2
Ring B						
Re	32.0	14.3	53.8	78.3	7.6	14.1
TS	30.4	20.7	48.9	86.8	12.8	0.4
Pr	32.8	14.1	53.1	90.1	2.4	7.5
			Reaction R2			
Ring A						
Re	99.0	0.2	0.8	34.0	37.0	29.1
TS	80.9	1.6	17.5	—	—	—
Pr	65.5	3.6	30.9	34.2	44.6	21.2
Ring B						
Re	39.8	4.4	55.8	82.6	4.7	12.7
TS	40.1	9.7	50.2	—	—	—
Pr	41.6	16.8	41.6	97.3	0.3	2.4
			Reaction R3			
Ring A						
Re	99.2	0.7	0.1	36.8	30.9	32.3
TS	73.7	9.4	16.8	—	—	—
Pr	57.5	13.1	29.4	33.5	45.5	21.0
Ring B						
Re	39.3	0.3	60.4	63.9	16.1	20.0
TS	43.5	15.5	41.0	—	—	—
Pr	44.8	23.9	31.3	97.7	0.0	2.3

Notes: [a]For Step 1 Re corresponds to **S**, TS to **TS (SIa)** and Pr to **Ia**; for Step 2 Re corresponds to **Ib**, TS to **TS (IbE)** and Pr to **E**.

(a) Puckering analysis for Step 1

(b) Puckering analysis for Step 2

Fig. 6. (Color online) Decomposition of the reaction curvature into puckering components for rings A and B for reaction R1; (a) Step 1 and (b) Step 2. The borders of the reaction phases are indicated by vertical dashed lines at curvature minimums $M1$, $M2$, $M3$, etc. and the curvature maximums are indicated by $K1$, $K2$, $K3$, etc. The reaction phases are indicated by the blue numbers. The TS at $s = 0$ amu$^{1/2}$ Bohr is also indicated by a vertical dotted line. The gray bar indicates the chemical phase.

it is easier for ring B to adjust to its final conformation in 4-androstene-3,17-dione **E**.

NBO charges and charge transfer. In this section we discuss how the charge distribution changes during the isomerization process, i.e., when the proton migrates from the ring A of the steroid molecule to the deprotonated side chain of aspartic acid in Step 1, followed in Step 2 by the back-transfer of the same proton from the acid to the ring B of the steroid molecule. Figure 7 presents the NBO atomic charges along the reaction path for the migrating proton, α- and γ carbon atoms of the steroid molecule (C_a and C_b in Fig. 7, respectively) and the oxygen of the aspartic/formic acid accepting the migrating proton. In addition, the total charge of the steroid with and without the migrating H atoms and that of the deprotonated acid are plotted as

well along the reaction path in order to reflect the charge transfer between these two entities. (Fig. S4, Supporting Materials, shows in addition the NBO charge differences between the protonated steroid moiety and the deprotonated acid for Step 1 of the reactions R1–R3 along the reaction path.)

In both reactions, R1 and R2, the migrating H-atom keeps a positive charge of 0.35 e during the first reaction phases of Step 1. At the end of chemical phase 3, the positive charge starts to slightly increase until shortly after the TS in phase 4 its final value of 0.5 e in **Ia** is reached, where the hydrogen atom is bonded to the acid. In phase 3 of Step 2 the positive charge starts to decrease until it reaches its final value of 0.3 e in **E** at
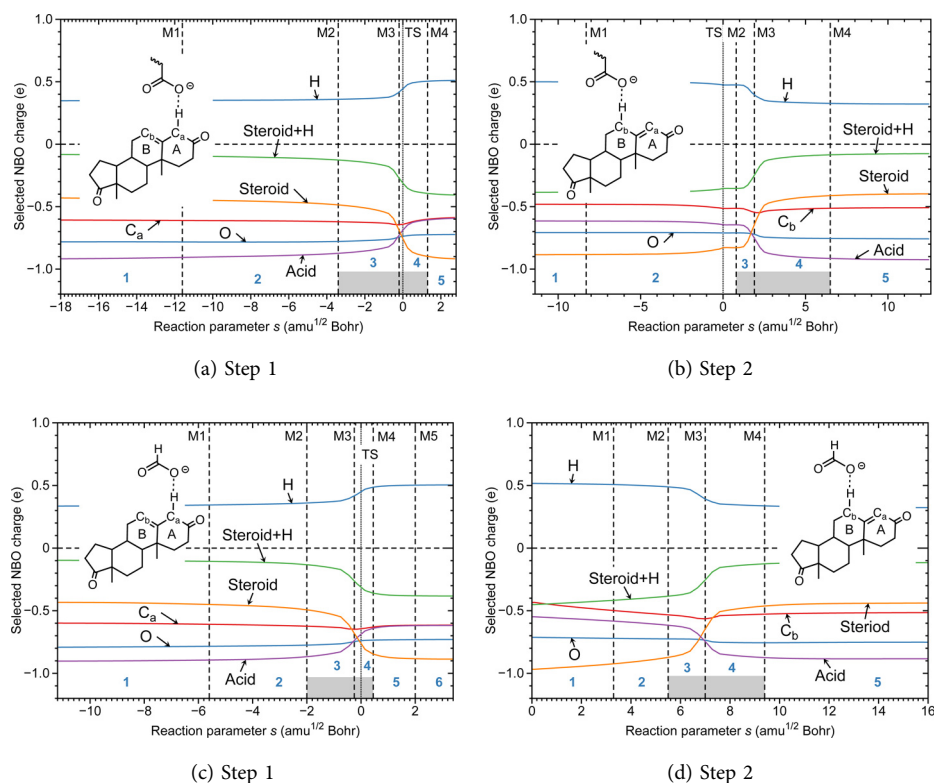
Fig. 7. (Color online) The NBO charges of selected atoms and overall charge of the steroid molecule and the interacting acid along the reaction path; (a) and (b) Step 1 and Step 2 of reaction R1, respectively; (c) and (d) Step 1 and Step 2 of reaction R2. Because Step 2 of R2 is barrier-less, the reaction path corresponds to a downhill path starting from **Ib**. The borders of the reaction phases are indicated by vertical dashed lines at curvature minimums $M1$, $M2$, $M3$, etc. The reaction phases are indicated by the blue numbers. The TS at $s = 0$ amu$^{1/2}$ Bohr is also indicated by a vertical dotted line. The gray bar indicates the chemical phase.

the beginning of phase 4. Both α- and γ-carbon atoms and the O atom are negatively charged throughout both the steps; with only marginal changes, i.e., the overall change of the charge of both, steroid and acid along during the isomerization process is determined by the charge of the migrating H-atom. At the beginning of Step 1 of reaction R1, the steroid including the migrating H-atom carries -0.1 e and the deprotonated Asp38 of -0.9 e of the overall negative charge of -1 e at the intermediate **Ia** the roles are switched, the steroid has a negative charge of -0.9 e. In Step 2 the reverse charge transfer takes places, so that at the end of the isomerization the deprotonated acid has a negative charge of -0.9 e again. The same trends are observed for the gas phase phase reaction R2 as revealed by Fig. 7. This shows that specific electrostatic field effects and enhanced charge transfer in the enzyme can be excluded.

Local Mode Analysis. Finally, we address the remaining two questions (i) TS stabilization via strong hydrogen bonding and (ii) the role of Tyr14 and Asp99 via a comprehensive local mode analysis. Table 4

summarizes bond length R, local mode force constant k^a, energy density at the bond critical point H_ρ, and bond strength order BSO for the C–H and O–H bonds primarily involved in the isomerization reactions R1–R3 taken at the stationary points. Figure 8 shows in addition bond lengths (black color) and BSO values (brown color) also for additional C–H, O–H, C–O and C–C bonds at the stationary points of Steps 1 and 2 of the isomerization reaction R1 in the enzyme.

In the starting, van der Waals complex **S**, C–O bond of deprotonated Asp38 acid is in closer contact with the migrating H-atom which is only slightly longer and weaker than the other C–O bond of the carboxylate anion part ($R = 1.260$ Å, BSO $= 1.566$ versus $R = 1.256$ Å, BSO $= 1.612$, respectively). In **TS(SIa)** the difference between the two CO bonds increases and in the intermediate **Ia** one can speak of a C–O single bond and a C–O double bond as depicted in Fig. 8 with ($R = 1.319$ Å, BSO $= 1.269$ versus $R = 1.214$ Å, BSO $= 1.905$, respectively). At the same time the OH– bond with the migrating H-atom changes from a weak

Table 4. Bond length R, local mode force constant k^a, energy density at the bond critical point H_ρ, and bond strength order BSO for the C–H and O–H bonds involved in the isomerization reactions R1–R3 taken at the stationary points: 5-androstene complex S, TS(SIa), intermediates Ia and Ib, TS(IbE) and 4-androstene complex E[a].

| | R (Å) | | | | | | k^a (mDyn/Å) | | | | | |
Reaction	S	TS(SIa)	Ia	Ib	TS(IbE)	E	S	TS(SIa)	Ia	Ib	TS(IbE)	E
R1												
C_a–H	1.119	1.474	1.928	2.995	3.001	2.962	4.078	0.488	0.149	0.171	0.184	0.518
C_b–H	3.069	3.340	3.584	1.839	1.679	1.106	0.576	0.267	0.134	0.066	0.091	4.593
O–H	1.999	1.208	1.025	1.049	1.105	2.081	0.158	0.513	3.131	1.104	0.275	0.144
R2												
C_a–H	1.107	1.490	1.784	3.725	—	3.157	4.562	0.398	0.185	0.048	—	0.508
C_b–H	3.172	3.253	3.397	2.622	—	1.105	0.532	0.151	0.102	0.122	—	4.595
O–H	2.119	1.181	1.047	0.992	—	2.186	0.090	0.508	2.063	6.051	—	0.066
R3												
C_a–H	1.107	1.504	1.800	3.059	—	3.121	4.601	0.568	0.196	0.078	—	0.471
C_b–H	3.148	3.246	3.385	1.865	—	1.102	0.502	0.126	0.078	0.163	—	4.921
O–H	2.248	1.165	1.036	1.024	—	2.388	0.056	0.638	2.454	2.966	—	0.074

| | H_ρ (Hartree/Bohr^3) | | | | | | BSO | | | | | |
Reaction	S	TS(SIa)	Ia	Ib	TS(IbE)	E	S	TS(SIa)	Ia	Ib	TS(IbE)	E
R1												
C_a–H	−0.2671	−0.0615	−0.0064	—	—	—	0.881	0.329	0.190	0.203	0.210	0.339
C_b–H	—	—	—	−0.0102	−0.0236	−0.2846	0.356	0.249	0.181	0.130	0.151	0.931
O–H	−0.0011	−0.1863	−0.4531	−0.4013	−0.3093	−0.0011	0.241	0.368	0.706	0.485	0.294	0.233
R2												
C_a–H	−0.2805	−0.0555	−0.0123	—	—	—	0.928	0.300	0.210	0.113	—	0.336
C_b–H	—	—	—	0.0000	—	−0.2848	0.343	0.191	0.160	0.173	—	0.931
O–H	−0.0006	−0.2214	−0.4060	−0.5397	—	−0.0007	0.196	0.367	0.608	0.896	—	0.176
R3												
C_a–H	−0.276	−0.0514	−0.0109	—	—	—	0.932	0.353	0.216	0.141	—	0.324
C_b–H	—	—	—	−0.0075	—	−0.2819	0.334	0.176	0.141	0.198	—	0.961
O–H	−0.001	−0.2413	−0.4304	−0.4590	—	−0.0002	0.166	0.398	0.647	0.693	—	0.183

Notes: [a]R, k^a, and H_ρ of the C–H bond in CH_4, are 1.092 Å, 5.362 mDyn/Å, and −0.2823 Hartree/Bohr^3, respectively. R, k^a, and H_ρ of the O–H bond in H_2O, are 0.965 Å, 8.208 mDyn/Å, and −0.5878 Hartree/Bohr^3, respectively.

interaction in **S** to a covalent OH-bond in **Ia** reflecting the drastic change of the R values (1.999 Å versus 1.025 Å, respectively, and the corresponding BSO values of 0.241 versus 0.706, respectively). Synchronously, C_αH bond becomes longer and weaker, with $R = 1.119$ Å, BSO = 0.881 in **S** versus $R = 1.928$ Å, BSO = 0.190 in **Ia**, respectively. The B CC double bond becomes slightly longer and the C_αC bonds of ring A slightly shorter. The CO double bond in proximity to Asp99 and Tyr14 becomes longer and weaker $R = 1.231$ Å, BSO = 1.820 in **S** versus $R = 1.266$ Å, BSO = 1.554 in **Ia**, respectively. However, hydrogen bonding between the substrate carbonyl oxygen and Asp99 and Tyr14 changes only marginally, (Asp99: $R = 1.856$ Å, BSO = 0.306 in **S** versus $R = 1.797$ Å, BSO = 0.354 in **Ia**, respectively; Tyr14: $R = 1.825$ Å, BSO = 0.345 in **S** versus $R = 1.768$ Å, BSO = 0.392 in **Ia**, respectively), therefore the suggested strong

catalytic activity of Asp99 and Tyr14 can be excluded, which is in line with our observation that the energetics and mechanism in both gas phase and enzyme are pretty similar. Along the same lines, there is no particularly strong hydrogen bonding in the TSs, which would explain the low activation barrier.

Bond length and bond strength changes in Step 2 follow a somewhat different pattern as shown in Fig. 8, where now the focus is on both ring A and ring B. In the starting intermediate **Ib**, the C–O bonds of the protonated Asp38 acid reflect double and single bond character with $R = 1.224$ Å, BSO = 1.762 versus $R = 1.303$ Å, BSO = 1.240, respectively. In the final complex **E**, the two CO bond of the deprotonated Asp38 acid are again fairly equal with $R = 1.264$ Å, BSO = 1.563 versus $R = 1.249$ Å, BSO = 1.657, respectively. At the same time the covalent OH-bond with the migrating H-atom changes back to a weak
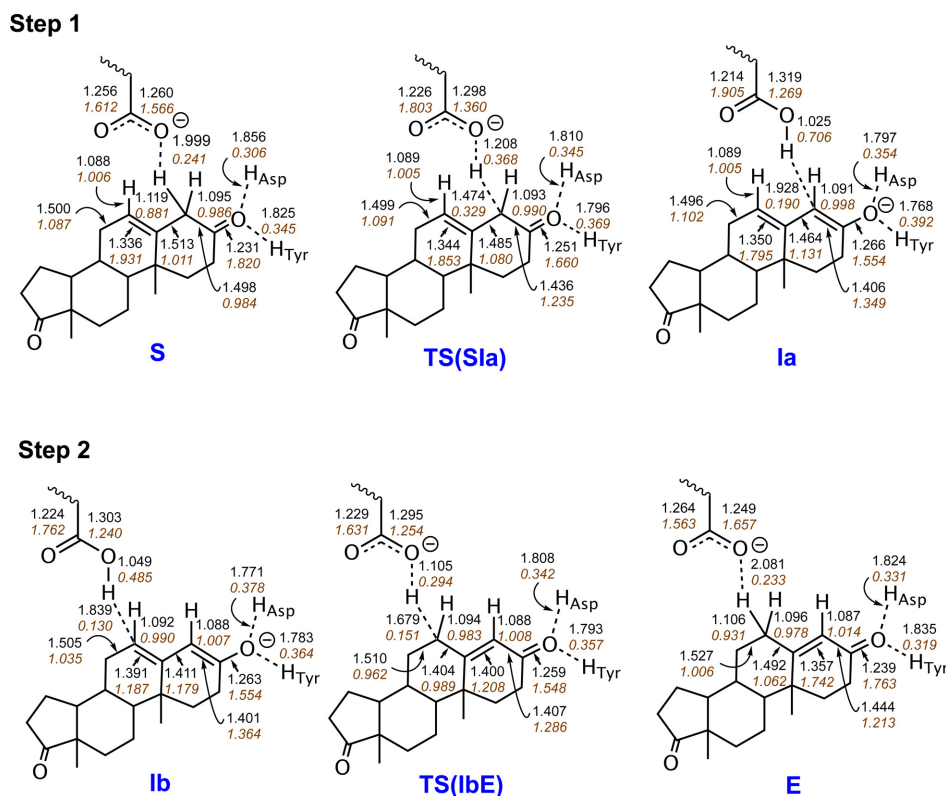
Fig. 8. (Color online) Bond lengths in Å (black color) and BSO values (brown color) for the selected C–H, O–H, C–O and C–C bonds at the stationary points of Steps 1 and 2 of the isomerization reaction R1 in the enzyme.

interaction, with $R = 1.049$ Å, BSO $= 0.485$ in **Ib** versus $R = 2.081$ Å, BSO $= 0.233$ in **E**, respectively. Synchronously, the $C_\gamma H$ bond becomes shorter and stronger with $R = 1.839$ Å, BSO $= 0.130$ in **Ib** versus $R = 1.106$ Å, BSO $= 0.931$ in **E**, respectively. As in Step 1 hydrogen bonding between the substrate carbonyl oxygen and Asp99 and Tyr14 changes only marginally, (Asp99: $R = 1.771$ Å, BSO $= 0.378$ in **Ib** versus $R = 1.824$ Å, BSO $= 0.331$ in **E**, respectively; Tyr14: $R = 1.783$ Å, BSO $= 0.364$ in **Ib** versus $R = 1.835$ Å, BSO $= 0.319$ in **E**, respectively). In contrast to Step 1 the CC bonds in both ring A and B change length and strength to accommodate the necessary double bond shift leading to the final 4-androstene-3,17-dione **E**.

In Figs. 9 and 10, general bond length/strength changes for the C–H and O–H bonds primarily involved in the isomerization process are visualized for all three reactions R1–R3 based on the data of Table 4. As obvious from Fig. 9(a), C_α–H bonds in **S** and the C_γ–H bonds in **E** are the strongest C–H bonds with a bond strength close to that found in CH_4 (k^a values are in the range between 4.078 mDyn/Å and 4.601 mDyn/Å compared to the $k^a(CH)$ value of 5.362 mDyn/Å for

CH_4), whereas the corresponding C–H bonds of the intermediates **Ia** and **Ib** are the weakest (**Ia**: k^a values in the range of 0.149–0.196 mDyn/Å and **Ib**: k^a values in the range of 0.171–0.048 mDyn/Å). C–H bond strengths at the transition states of Step 1 cover an intermediate range. **TS (IbE)** of R1 (Step 2 of reactions R2 and R3 is barrier-less) falls into the range of the weak C–H bond of the intermediates, reflecting that because of the small barrier and strong exothermicity, the TS is close to the reactant **Ib** in line with the Hammond–Leffler postulate.[141] Figure 9(b) shows the corresponding O–H bond strengths which are complementary to those of the C–H bonds. Weakest O–H bonds are found for the 5-androstene-3,17-diones **S** and 4-androstene-3,17-diones **E** in which Asp38/formic acid is deprotonated, strongest O–H bonds are found for the intermediates, which are generally weaker that the O–H bond in water ($k^a(OH) = 8.208$ mDyn/Å). They show a larger spread of k^a values (i.e., range between 1.104 and 6.051 mDyn/Å) than those of the C–H bonds. This indicates that the O–H bonds are more sensitive to the environment than the C–H bonds.

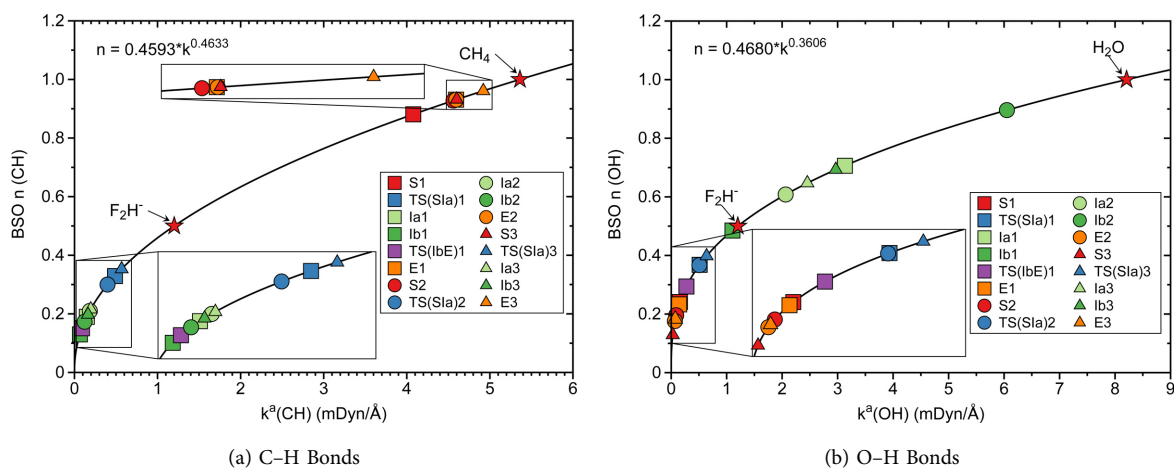Figures 10(a) and 10(b) show the correlation between bond strength and bond length for C–H and

Fig. 9. (Color online) (a) BSO n(CH) as a function of the local mode force constant k^a(CH), $C_\alpha H$ bonds for Step 1 and $C_\gamma H$ bonds for Step 2 of reactions R1–R3; (b) BSO n(OH) as a function of the local mode force constant k^a(OH) for Steps 1 and 2 of reactions R1–R3, calculated from the power relationship described in the text. Naming of the symbols in the legend is according to Fig. 1.
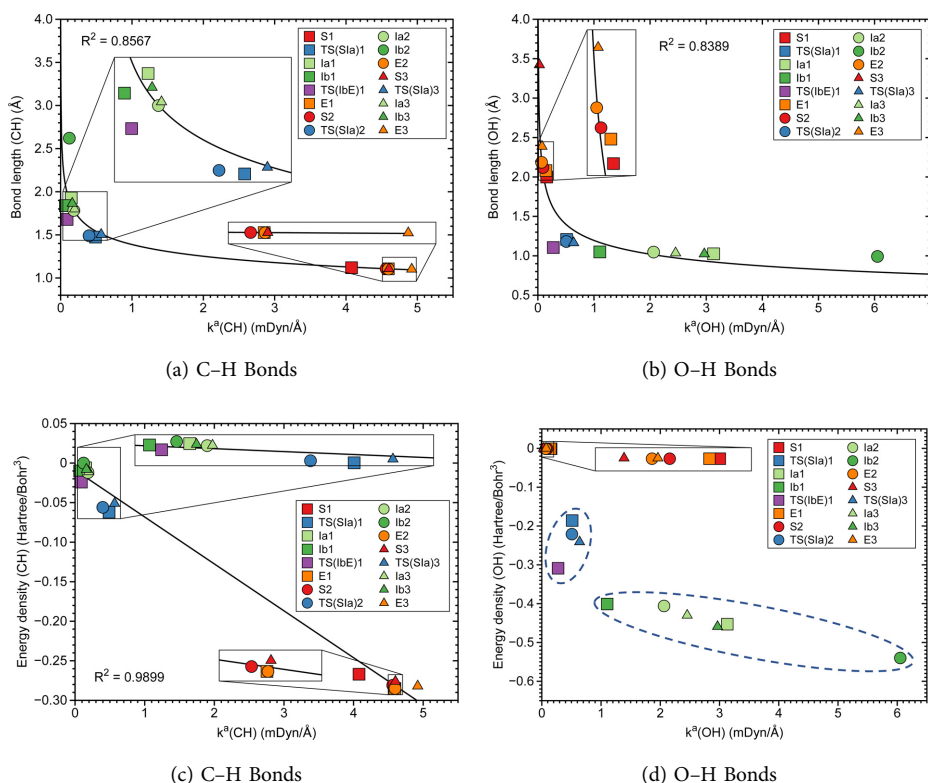

Fig. 10. (Color online) (a) Correlation between R(CH) and k^a(CH); (b) Correlation between R(OH) and k^a(OH); (c) Correlation between H_ρ(CH) and k^a(CH); (d) Correlation between H_ρ(OH) and k^a(OH) for Steps 1 and 2 of reactions R1–R3. Naming of the symbols in the legend is according to Fig. 1.

O–H bonds, respectively. In both cases there is a moderate correlation ($R^2 = 0.8567$ for C–H bonds, $R^2 = 0.8389$ for O–H bonds) reflecting the general trend that shorter bonds are the stronger bonds, which is not always true.[86,142] In Figs. 10(c) and 10(d) the correlation between bond strength and the energy density H_ρ for C–H and O–H bond, respectively, is depicted. All C–H bonds of intermediates **Ia** and **Ib**,

TS(SIa) and **TS(IbE)** have H_ρ values close to zero, i.e., no predominant covalent character, whereas the C–H bonds of **S** and **E** complexes are strongly covalent, the correlation between H_ρ(CH) and k^a(CH) is significant ($R^2 = 0.8567$). This no longer holds for the O–H bonds, as revealed in Fig. 10(d). There are three clusters of O–H bonds, one compact cluster formed by the weak O–H interactions in **S** and **E** complexes with H_ρ values close to zero, i.e., no predominant covalent character, second cluster formed by the TSs, with moderate covalent character, and a third cluster spreading over a large k^a range with substantial covalent character formed by the protonated intermediates. Again, the large spread of values and the missing correlation reflect that the O–H bonds are more sensitive to the environment such as solvent than their CH counterparts, which is not well represented by H_ρ, a property taken at a single point on the bond path, whereas the local mode force constant as a second-order properties sensitively picks up the environment between both atoms forming the bond/interaction under consideration.

4. CONCLUSIONS AND OUTLOOK

We investigated in this work the two-step isomerization of 5-androstene-3,17-dione to 4-androstene-3,17-dione in WT KSI (reaction R1) utilizing as a novel toolbox the combination of URVA, LMA and ring puckering. The focus was on shedding more light into the currently open questions how the exceptional catalytic power of KSI is reflected in the mechanism, in particular (i) how do different chemical events such as bond formation/breaking, rehybridization and conformational changes contribute to the activation barrier and (ii) although in both steps C–H bonds are broken, C and O atoms are rehybridized, why is the second step obviously much more effortless than the first step? To elucidate the catalytic effect of Asp38 in the protein and to test the postulated shielding of the enzyme active site pocket conserving the migrating hydrogen from interactions with surrounding bulk water, we also modeled the reaction in the gas phase (reaction R2) and in aqueous solution (reaction R3), simulating Asp38 with formic acid. This led to the following findings:

- The activation enthalpies of Step 1 in the enzyme and in the gas phase are very similar (6.6 kcal/mol, R1 versus 6.1 kcal/mol, R2, respectively) confirming Talalay's hypothesis that the enzyme pocket shields the migrating hydrogen atom. This is also fully in line with our observation that in the aqueous solution allowing solvent solute interaction the activation

barriers increases considerably (6.1 kcal/mol, R2 versus 11.4 kcal/mol, R3, respectively).

- URVA identifies simultaneous breakage of the C_α–H bond and O–H bond formation with the catalytic acid, leading to an intermediate with the acid positioned over ring A as the major chemical events of the first reaction step. Via a barrier-less shift, a second intermediate is formed with the acid being positioned over ring B (see Fig. S5, supporting materials). Then, according to URVA, breakage of the intermediate O–H bond and the formation of the new C_γ–H bond accompanied by a double bond shift in rings A and B form the major chemical events of the second reaction step, which is facilitated by favorable ring puckering.

- In 5-androstene-3,17-dione, the α-carbon of ring A is sp^3 hybridized. Consequently, ring A has a predominant chair conformation in both gas phase, solution and enzyme (the value for the enzyme is somewhat smaller, caused by the space confinement in the enzyme pocket). On the other hand, in 4-androstene-3,17-dione, the γ-carbon of ring B is sp^3 hybridized and has a predominant chair conformation. Obviously, ring B has more flexibility to adjust to the chair form than ring A. The γ-carbon of ring B in reactant **S** and the α-carbon of product **E** in ring A are sp^2 hybridized. Cyclohexene and cyclohexenone rings are known to prefer a half-chair form, which is confirmed by our analysis revealing an almost equal admixture of chair, boat and Twist-boat conformations found for **E**. This indicates that the γ-carbon of ring B has already a dominant sp^3 hybridization, facilitating the proton transfer and in this way lowering the activation energy of Step 2.

- C_a–H bond cleavage and formation of the intermediate O–H bond with the acid proceed in the gas phase with the same mechanism as in the enzyme; i.e., starting with conformational adjustments in phases 1 and 2 making up 4.1 kcal/mol of the activation energy (44%) followed by the start of C_a–H bond cleavage and O–H bond formation (5.5 kcal/mol). The overall mechanism remains the same in aqueous solution, the major difference is that C_a–H bond cleavage is more difficult; the contribution of phases 3 and 4 to the barrier is increased (67%). This reflects that the catalytic power of the acid is reduced because of interaction with the solvent.

- In both steps, rehybridization as reflected by the pyramidalization angles contributes to the chemical phases (phases 3 and 4, curvature peaks $K3$ and $K4$ in Step 1 and curvature peaks $K2$ and $K3$ in Step 2). The same features were found for the gas phase and

aqueous solution reactions, amplifying that the overall mechanism is the same in all three media. In addition, specific electrostatic field effects and enhanced charge transfer in the enzyme can be excluded according to our NBO data, monitored along the reaction path.

- The LMA analysis performed at the stationary points of both isomerization steps shows that in the enzyme (i) there is no special H-bonding with Asp99 and Tyr14, excluding their catalytic activity, and (ii) there is no strong hydrogen bonding in the TS, which could account for lowering the activation barrier.

In summary, our study quantifies Talaly's postulated role of the enzymatic activity of KSI shielding the migrating hydrogen at the starting 4-position (i.e., α-carbon) guiding it directly to the 6-position (γ-carbon) of the steroid. Furthermore, it provides a clear picture of the mechanistic features and details of the isomerization process, which will hopefully inspire similar investigations of other important enzymatic reactions.

ACKNOWLEDGMENTS

SUPPORTING MATERIALS

The following supporting materials are available free of charge.

- Table S1. Comparison of the energetics of reactions R2 and R3 based on 6–31G(d,p) and 6–311G(d,p) basis sets.
- Fig. S1. Simplified energy profiles for reactions R1–R3.
- Fig. S2. Decomposition of the reaction path curvature into pyramidalization angle components for R2.
- Fig. S3. Decomposition of the reaction path curvature into ring puckering components for R2 and R3.
- Fig. S4. NBO charge differences along the reaction paths.
- Fig. S5. Overlay of the structures of the intermediates for the reaction R1.
- Fig. S6 and S7. Decomposition of the reaction path direction into selected components for reactions R1–R3.

References

1. Kedzierski, P.; Zaczkowska, M.; Sokalski, W. A. Extreme Catalytic Power of Ketosteroid Isomerase Related to the Reversal of Proton Dislocations in Hydrogen-Bond Network. *J. Phys. Chem. B* **2020**, *124*, 3661–3666.

2. Yabukarskia, F.; Bielb, J. T.; Pinneya, M. M.; Doukov, T.; Powers, A. S.; Fraser, J. S.; Herschlag, D. Assessment of Enzyme Active Site Positioning and Tests of Catalytic Mechanisms through X-ray–Derived Conformational Ensembles. *Proc. Natl. Acad. Sci.* **2020**, *117*, 33204–33215.

3. Hawkinson, D. C.; Eames, T. C. M.; Pollack, R. M. Energetics of 3-Oxo-Δ^5-Steroid Isomerase — Source of the Catalytic Power of the Enzyme. *Biochemistry* **1991**, *30*, 10849–10858.

4. Kemp, M. T.; Lewandowski, E. M.; Chen, Y. Low Barrier Hydrogen Bonds in Protein Structure and Function. *Biochim. Biophys. Acta – Proteins Proteom.* **2021**, *1869*, 140557–1–140557–9.

5. Hennefarth, M. R.; Alexandrova, A. N. Advances in Optimizing Enzyme Electrostatic Preorganization. *Curr. Opin. Struct. Biol.* **2022**, *72*, 1–8.

6. Leonard, N. G.; Dhaoui, R.; Chantarojsiri, T.; Yang, J. Y. Electric Fields in Catalysis: From Enzymes to Molecular Catalysts. *ACS Catal.* **2021**, *11*, 10923–10932.

7. Wu, Y.; Fried, S. D.; Boxer, S. G. A Preorganized Electric Field Leads to Minimal Geometrical Reorientation in the Catalytic Reaction of Ketosteroid Isomerase. *J. Am. Chem. Soc.* **2020**, *142*, 9993–9998.

8. Fried, S. D.; Boxer, S. G. Evaluation of the Energetics of the Concerted Acid-Base Mechanism in Enzymatic Catalysis: The Case of Ketosteroid Isomerase. *J. Phys. Chem. B* **2012**, *116*, 690–697.

9. Welborn, V. V.; Head-Gordon, T. Fluctuations of Electric Fields in the Active Site of the Enzyme Ketosteroid Isomerase. *J. Am. Chem. Soc.* **2019**, *141*, 12487–12492.

10. MacLachlan, J.; Wotherspoon, A. T. L.; Ansell, R. O.; Brooks, C. J. W. Cholesterol Oxidase: Sources, Physical Properties and Analytical Applications. *J. Steroid Biochem. Mol. Biol.* **2000**, *72*, 169–195.

11. Talalay, P. A Fascination with Enzymes: The Journey not the Arrival Matters. *J. Biol. Chem.* **2005**, *280*, 28829–28847.

12. Pollack, R. M. Enzymatic Mechanisms for Catalysis of Enolization: Ketosteroid Isomerase. *Bioorg. Chem.* **2004**, *32*, 341–353.

13. Whittington, C.; Latham, J.; Offenbacher, A. R. *Tunneling through the Barriers: Resolving the Origins of the Activation of C–H Bonds Catalyzed by Enzymes*, Vol. 1357, American Chemical Society, Washington DC, 2020, pp. 139–160.

14. Wang, S.-F.; Kawahara, F. S.; Talalay, P. The Mechanism of the Δ^5-3-Ketosteroid Isomerase Reaction:

Absorption and Fluorescence Spectra of Enzyme-Steroid Complexes. *J. Biol. Chem.* **1963**, *238*, 576–585.

15. Pollack, R. M.; Thornburg, L. D.; Wu, Z. R.; Summers, M. F. Mechanistic Insights from the Three-Dimensional Structure of 3-Oxo-Δ^5-steroid Isomerase. *Arch. Biochem. Biophys.* **1999**, *370*, 9–15.

16. Ha, N.-C.; Choi, G.; Choi, K. Y.; Oh, B.-H. Structure and Enzymology of Δ^5-3-Ketosteroid Isomerase. *Curr. Opin. Struct. Biol.* **2001**, *11*, 674–678.

17. Talalay, P.; Wang, V. S. Enzymic Isomerization of Δ^5-3-Ketosteroids. *Biochim. Biophys. Acta* **1955**, *18*, 300–301.

18. Zhao, Q.; Abeygunawardana, C.; Talalay, P.; Mildvan, A. S. NMR Evidence for the Participation of a Low-barrier Hydrogen Bond in the Mechanism of Δ^5-3-Ketosteroid Isomerase. *Proc. Natl. Acad. Sci. USA* **1996**, *93*, 8220–8224.

19. Zhao, Q.; Abeygunawardana, C.; Gittis, A. G.; Mildvan, A. S. Hydrogen Bonding at the Active Site of Δ^5-3-Ketosteroid Isomerase. *Biochemistry* **1997**, *36*, 14616–14626.

20. Wang, L.; Fried, S. D.; Markland, T. E. Proton Network Flexibility Enables Robustness and Large Electric Fields in the Ketosteroid Isomerase Active Site. *J. Phys. Chem. B* **2017**, *121*, 9807–9815.

21. Park, H.; Merz, K. M. Jr. Molecular Dynamics and Quantum Chemical Studies on the Catalytic Mechanism of Δ^5-3-Ketosteroid Isomerase: The Catalytic Diad versus the Cooperative Hydrogen Bond Mechanism. *J. Am. Chem. Soc.* **2003**, *125*, 901–911.

22. Feierberg, I.; Aqvist, J. The Catalytic Power of Ketosteroid Isomerase Investigated by Computer Simulation. *Biochemistry* **2002**, *41*, 15728–15735.

23. Pan, Y.; McAllister, M. A. Theoretical Investigation of the Role of Hydrogen Bonding During Ketosteroid Isomerase Catalysis. *J. Mol. Struct. (Theochem)* **2000**, *504*, 29–33.

24. Childs, W.; Boxer, S. G. Proton Affinity of the Oxyanion Hole in the Active Site of Ketosteroid Isomerase. *Biochemistry* **2010**, *49*, 2725–2731.

25. Hanoian, P.; Sigala, P. A.; Herschlag, D.; Hammes-Schiffer, S. Hydrogen Bonding in the Active Site of Ketosteroid Isomerase: Electronic Inductive Effects and Hydrogen Bond Coupling. *Biochemistry* **2010**, *49*, 10339–10348.

26. Sigala, P. A.; Kraut, D. A.; Caaveiro, J. M. M.; Pybus, B.; Ruben, E. A.; Ringe, D.; Petsko, G. A.; Herschlag, D. Testing Geometrical Discrimination within an Enzyme Active Site: Constrained Hydrogen Bonding in the Ketosteroid Isomerase Oxyanion Hole. *J. Am. Chem. Soc.* **2008**, *130*, 13696–13708.

27. Cha, H. J.; Jang, D. S.; Jeong, J.-H.; Hong, B. H.; Yun, Y. S.; Shin, E. J.; Choi, K. Y. Role of Conserved Met112 Residue in the Catalytic Activity and Stability of Ketosteroid Isomerase. *Biochim. Biophys. Acta* **2016**, *1864*, 1322–1327.

28. Pinney, M. M.; Natarajan, A.; Yabukarski, F.; Sanchez, D. M.; Liu, F.; Liang, R.; Doukov, T.; Schwans, J. P.; Martinez, T. J.; Herschlag, D. Structural Coupling Throughout the Active Site Hydrogen Bond Networks of Ketosteroid Isomerase and Photoactive Yellow Protein. *J. Am. Chem. Soc.* **2018**, *140*, 9827–9843.

29. Wu, Y.; Fried, S. D.; Boxer, S. G. Dissecting Proton Delocalization in an Enzyme's Hydrogen Bond Network with Unnatural Amino Acids. *Biochemistry* **2015**, *54*, 7110–7119.

30. Kamerlin, S. C. L.; Sharma, P. K.; Chu, Z. T.; Warshel, A. Ketosteroid Isomerase Provides Further Support for the Idea that Enzymes Work by Electrostatic Preorganization. *Proc. Natl. Acad. Sci.* **2010**, *107*, 4075–4080.

31. Warshel, A.; Sharma, P. K.; Chu, Z. T.; Aqvist, J. Electrostatic Contributions to Binding of Transition State Analogues Can be Very Different from the Corresponding Contributions to Catalysis: Phenolates Binding to the Oxyanion Hole of Ketosteroid Isomerase. *Biochemistry* **2007**, *46*, 1466–1476.

32. Fuller, J.; Wilson, T. R.; Eberhart, M. E.; Alexandrova, A. N. Charge Density in Enzyme Active Site as a Descriptor of Electrostatic Preorganization. *J. Chem. Inf. Model.* **2019**, *59*, 2367–2373.

33. Wang, X.; He, X. An Ab Initio QM/MM Study of the Electrostatic Contribution to Catalysis in the Active Site of Ketosteroid Isomerase. *Molecules* **2018**, *23*, 2410–2426.

34. Zoi, I.; Antoniou, D.; Schwartz, S. D. Electric Fields and Fast Protein Dynamics in Enzymes. *J. Chem. Phys. Lett.* **2017**, *8*, 6165–6170.

35. Beker, W.; van der Kamp, M. W.; Mulholland, A. J.; Sokalski, W. A. Rapid Estimation of Catalytic Efficiency by Cumulative Atomic Multipole Moments: Application to Ketosteroid Isomerase Mutants. *J. Chem. Theory Comput.* **2017**, *13*, 945–955.

36. Wang, L.; Fried, S. D.; Boxer, S. G.; Markland, T. E. Quantum Delocalization of Protons in the Hydrogen-bond Network of an Enzyme Active Site. *Proc. Natl. Acad. Sci.* **2014**, *111*, 18454–18459.

37. van der Kamp, M. W.; Chaudret, R.; Mulholland, A. J. QM/MM Modelling of Ketosteroid Isomerase Reactivity Indicates that Active Site Closure is Integral to Catalysis. *FEBS J.* **2013**, *280*, 3120–3131.

38. Layfield, J. P.; Hammes-Schiffer, S. Calculation of Vibrational Shifts of Nitrile Probes in the Active Site of Ketosteroid Isomerase upon Ligand Binding. *J. Am. Chem. Soc.* **2013**, *135*, 717–725.

39. Somarowthu, S.; Brodkin, H. R.; D'Aquino, J. A.; Ringe, D.; Ondrechen, M. J.; Beuning, P. J. A Tale of Two Isomerases: Compact versus Extended Active Sites in Ketosteroid Isomerase and Phosphoglucose Isomerase. *Biochemistry* **2011**, *50*, 9283–9295.

40. Chakravorty, D. K.; Soudackov, A. V.; Hammes-Schiffer, S. Hybrid Quantum/Classical Molecular

Dynamics Simulations of the Proton Transfer Reactions Catalyzed by Ketosteroid Isomerase: Analysis of Hydrogen Bonding, Conformational Motions, and Electrostatics. *Biochemistry* **2009**, *48*, 10608–10619.

41. Wu, Y.; Boxer, S. G. A Critical Test of the Electrostatic Contribution to Catalysis with Noncanonical Amino Acids in Ketosteroid Isomerase. *J. Am. Chem. Soc.* **2016**, *138*, 11890–11895.

42. Fried, S. D.; Bagchi, S.; Boxer, S. G. Extreme Electric Fields Power Catalysis in the Active Site of Ketosteroid Isomerase. *Science* **2014**, *346*, 1510–1514.

43. Sigala, P. A.; Fafarman, A. T.; Bogard, P. E.; Boxer, S. G.; Herschlag, D. Do Ligand Binding and Solvent Exclusion Alter the Electrostatic Character within the Oxyanion Hole of an Enzymatic Active Site? *J. Am. Chem. Soc.* **2007**, *129*, 12104–12105.

44. Natarajan, A.; Schwans, J. P.; Herschlag, D. Using Unnatural Amino Acids to Probe the Energetics of Oxyanion Hole Hydrogen Bonds in the Ketosteroid Isomerase Active Site. *J. Am. Chem. Soc.* **2014**, *136*, 7643–7654.

45. Jha, S. K.; Ji, M.; Gaffney, K. J.; Boxer, S. G. Site-Specific Measurement of Water Dynamics in the Substrate Pocket of Ketosteroid Isomerase Using Time-Resolved Vibrational Spectroscopy. *J. Phys. Chem. B* **2012**, *116*, 11414–11421.

46. Jha, S. K.; Ji, M.; Gaffney, K. J.; Boxer, S. G. Direct Measurement of the Protein Response to an Electrostatic Perturbation that Mimics the Catalytic Cycle in Ketosteroid Isomerase. *Proc. Natl. Acad. Sci.* **2011**, *108*, 16612–16617.

47. Fafarman, A. T.; Sigala, P. A.; Schwans, J. P.; Fenn, T. D.; Herschlag, D.; Boxer, S. G. Quantitative, Directional Measurement of Electric Field Heterogeneity in the Active Site of Ketosteroid Isomerase. *Proc. Natl. Acad. Sci.* **2012**, *109*, E299–E308.

48. Fafarman, A. T.; Sigala, P. A.; Herschlag, D.; Boxer, S. G. Decomposition of Vibrational Shifts of Nitriles into Electrostatic and Hydrogen-Bonding Effects. *J. Am. Chem. Soc.* **2011**, *132*, 12811–12813.

49. Childs, W.; Boxer, S. G. Solvation Response along the Reaction Coordinate in the Active Site of Ketosteroid Isomerase. *J. Am. Chem. Soc.* **2010**, *132*, 6474–6480.

50. Yabukarski, F.; Biel, J. T.; Pinney, M. M.; Doukov, T.; Powers, A. S.; Fraser, J. S.; Herschlag, D. Assessing Positioning in Enzymatic Catalysis via Ketosteroid Isomerase Conformational Ensembles. *bioRxiv* **2019**, 786327.

51. Kraut, D. A.; Sigala, P. A.; Pybus, B.; Liu, C. W.; Ringe, D.; Petsko, G. A.; Herschlag, D. Testing Electrostatic Complementarity in Enzyme Catalysis: Hydrogen Bonding in the Ketosteroid Isomerase Oxyanion Hole. *PLoS Biol.* **2006**, *4*, 501–519.

52. Wu, Z. R.; Ebrahimian, S.; Zawrotny, M. E.; Thornburg, L. D.; Perez-Alvarado, G. C.; Brothers, P.; Pollack, R. M.; Summers, M. F. Solution Structure of 3-Oxo-Δ^5-Steroid Isomerase. *Science* **1997**, *276*, 415–418.

53. Hietala, J.; Vuori, A.; Johnsson, P.; Pollari, I.; Reutemann, W.; Kieczka, H. *Ullmann's Encyclopedia of Industrial Chemistry*, American Cancer Society, Atlanta, GA, 2016, pp. 1–22.

54. Kyte, J.; Doolittle, R. F. A Simple Method for Displaying the Hydropathic Character of a Protein. *J. Mol. Biol.* **1982**, *157*, 105–132.

55. Kraka, E.; Zou, W.; Tao, Y.; Freindorf, M. Exploring the Mechanism of Catalysis with the Unified Reaction Valley Approach (URVA) — A Review. *Catalysts* **2020**, *10*, 691.

56. Zou, W.; Sexton, T.; Kraka, E.; Freindorf, M.; Cremer, D. A New Method for Describing the Mechanism of a Chemical Reaction Based on the Unified Reaction Valley Approach. *J. Chem. Theory Comput.* **2016**, *12*, 650–663.

57. Kraka, E. Reaction Path Hamiltonian and the Unified Reaction Valley Approach. *WIREs: Comput. Mol. Sci.* **2011**, *1*, 531–556.

58. Joo, H.; Kraka, E.; Quapp, W.; Cremer, D. The Mechanism of a Barrierless Reaction: Hidden Transition State and Hidden Intermediates in the Reaction of Methylene with Ethene. *Mol. Phys.* **2007**, *105*, 2697–2717.

59. Makoś, M. Z.; Freindorf, M.; Tao, Y.; Kraka, E. Theoretical Insights into [NHC]Au(I) Catalyzed Hydroalkoxylation of Allenes: A Unified Reaction Valley Approach Study. *J. Org. Chem.* **2021**, *86*, 5714–5726.

60. Nanayakkara, S.; Freindorf, M.; Tao, Y.; Kraka, E. Modeling Hydrogen Release from Water with Borane and Alane Catalysts: A Unified Reaction Valley Approach. *J. Phys. Chem. A* **2020**, *124*, 8978–8993.

61. Tao, Y.; Zou, W.; Nanayakkara, S.; Kraka, E. PyVibMS: A PyMOL Plugin for Visualizing Vibrations in Molecules and Solids. *J. Mol. Model.* **2020**, *26*, 290–1–290–12.

62. Nanayakkara, S.; Kraka, E. A New Way of Studying Chemical Reactions: A Hand-in-hand URVA and QTAIM Approach. *Phys. Chem. Chem. Phys.* **2019**, *21*, 15007–15018.

63. Freindorf, M.; Tao, Y.; Sethio, D.; Cremer, D.; Kraka, E. New Mechanistic Insights into the Claisen Rearrangement of Chorismate — A Unified Reaction Valley Approach Study. *Mol. Phys.* **2018**, *117*, 1172–1192.

64. Freindorf, M.; Cremer, D.; Kraka, E. Gold(I)-Assisted Catalysis — A Comprehensive View on the [3,3]-Sigmatropic Rearrangement of Allyl Acetate. *Mol. Phys.* **2017**, *116*, 611–630.

65. Reis, M. C.; López, C. S.; Kraka, E.; Cremer, D.; Faza, O. N. Rational Design in Catalysis: A Mechanistic Study of β-Hydride Eliminations in Gold(I) and Gold (III) Complexes Based on Features of the Reaction Valley. *Inorg. Chem.* **2016**, *55*, 8636–8645.

66. Sexton, T.; Kraka, E.; Cremer, D. Extraordinary Mechanism of the Diels-Alder Reaction: Investigation of Stereochemistry, Charge Transfer, Charge Polarization, and Biradicaloid Formation. *J. Phys. Chem. A* **2016**, *120*, 1097–1111.

67. Cremer, D.; Kraka, E. From Molecular Vibrations to Bonding, Chemical Reactions, and Reaction Mechanism. *Curr. Org. Chem.* **2010**, *14*, 1524–1560.

68. Kraka, E.; Cremer, D. Computational Analysis of the Mechanism of Chemical Reactions in Terms of Reaction Phases: Hidden Intermediates and Hidden Transition States. *Acc. Chem. Res.* **2010**, *43*, 591–601.

69. Miller, W. H.; Handy, N. C.; Adams, J. E. Reaction Path Hamiltonian for Polyatomic Molecules. *J. Chem. Phys.* **1980**, *72*, 99–112.

70. Reed, A. E.; Curtiss, L. A.; Weinhold, F. Intermolecular Interactions from a Natural Bond Orbital, Donor-Acceptor Viewpoint. *Chem. Rev.* **1988**, *88*, 899–926.

71. Weinhold, F.; Landis, C. R. *Valency and Bonding: A Natural Bond Orbital Donor-Acceptor Perspective*, Cambridge University Press, Cambridge, England, 2003.

72. Cremer, D.; Pople, J. A. General Definition of Ring Puckering Coordinates. *J. Am. Chem. Soc.* **1975**, *97*, 1354–1358.

73. Zou, W.; Tao, Y.; Cremer, D.; Kraka, E. Systematic Description of Molecular Deformations with Cremer–Pople Puckering and Deformation Coordinates Utilizing Analytic Derivatives: Applied to Cycloheptane, Cyclooctane, and Cyclo[18]carbon. *J. Chem. Phys.* **2020**, *152*, 154107–1–54107–15.

74. Konkoli, Z.; Cremer, D. A New Way of Analyzing Vibrational Spectra. I. Derivation of Adiabatic Internal Modes. *Int. J. Quantum Chem.* **1998**, *67*, 1–9.

75. Konkoli, Z.; Larsson, J. A.; Cremer, D. A New Way of Analyzing Vibrational Spectra. II. Comparison of Internal Mode Frequencies. *Int. J. Quantum Chem.* **1998**, *67*, 11–27.

76. Konkoli, Z.; Cremer, D. A New Way of Analyzing Vibrational Spectra. III. Characterization of Normal Vibrational Modes in terms of Internal Vibrational Modes. *Int. J. Quantum Chem.* **1998**, *67*, 29–40.

77. Konkoli, Z.; Larsson, J. A.; Cremer, D. A New Way of Analyzing Vibrational Spectra. IV. Application and Testing of Adiabatic Modes within the Concept of the Characterization of Normal Modes. *Int. J. Quantum Chem.* **1998**, *67*, 41–55.

78. Cremer, D.; Larsson, J. A.; Kraka, E. New Developments in the Analysis of Vibrational Spectra: On the Use of Adiabatic Internal, Vibrational Modes, in *Theoretical and Computational Chemistry*, Parkanyi, C., ed., Elsevier, Amsterdam, 1998, pp. 259–327.

79. Kraka, E.; Zou, W.; Tao, Y. Decoding Chemical Information from Vibrational Spectroscopy Data: Local Vibrational Mode Theory. *WIREs: Comput. Mol. Sci.* **2020**, *10*, 1480.

80. Wilson, E.; Decius, J.; Cross, P. *Molecular Vibrations. The Theory of Infrared and Raman Vibrational Spectra*, McGraw-Hill, New York, 1955.

81. Zou, W.; Cremer, D. C_2 in a Box: Determining its Intrinsic Bond Strength for the $X^1\Sigma^+_g$ Ground State. *Chem. Eur. J.* **2016**, *22*, 4087–4097.

82. Delgado, A. A. A.; Humason, A.; Kalescky, R.; Freindorf, M.; Kraka, E. Exceptionally Long Covalent CC Bonds — A Local Vibrational Mode Study. *Molecules* **2021**, *26*, 950–1–950–25.

83. Kraka, E.; Larsson, J. A.; Cremer, D. Generalization of the Badger Rule Based on the Use of Adiabatic Vibrational Modes in Vibrational Modes in Computational IR Spectroscopy, in *Computational Spectroscopy*, Grunenberg, J., ed., Wiley, New York, 2010, pp. 105–149.

84. Kalescky, R.; Kraka, E.; Cremer, D. Identification of the Strongest Bonds in Chemistry. *J. Phys. Chem. A* **2013**, *117*, 8981–8995.

85. Kraka, E.; Cremer, D. Characterization of CF Bonds with Multiple-Bond Character: Bond Lengths, Stretching Force Constants, and Bond Dissociation Energies. *ChemPhysChem* **2009**, *10*, 686–698.

86. Kraka, E.; Setiawan, D.; Cremer, D. Re-Evaluation of the Bond Length-Bond Strength Rule: The Stronger Bond Is not Always the Shorter Bond. *J. Comput. Chem.* **2015**, *37*, 130–142.

87. Setiawan, D.; Sethio, D.; Cremer, D.; Kraka, E. From Strong to Weak NF Bonds: On the Design of a New Class of Fluorinating Agents. *Phys. Chem. Chem. Phys.* **2018**, *20*, 23913–23927.

88. Sethio, D.; Lawson Daku, L. M.; Hagemann, H.; Kraka, E. Quantitative Assessment of $B-B-B$, $B-H_b-B$, and $B-H_t$ Bonds: From BH_3 to $B_{12}H_{12}^{2-}$. *ChemPhysChem* **2019**, *20*, 1967–1977.

89. Freindorf, M.; Yannacone, S.; Oliveira, V.; Verma, N.; Kraka, E. Halogen Bonding Involving I_2 and d^8 Transition-Metal Pincer Complexes. *Crystals* **2021**, *11*, 373–1–373–21.

90. Oliveira, V.; Kraka, E.; Cremer, D. The Intrinsic Strength of the Halogen Bond: Electrostatic and Covalent Contributions Described by Coupled Cluster Theory. *Phys. Chem. Chem. Phys.* **2016**, *18*, 33031–33046.

91. Oliveira, V.; Kraka, E.; Cremer, D. Quantitative Assessment of Halogen Bonding Utilizing Vibrational Spectroscopy. *Inorg. Chem.* **2016**, *56*, 488–502.

92. Oliveira, V.; Cremer, D. Transition from Metal-Ligand Bonding to Halogen Bonding Involving a Metal as Halogen Acceptor: A Study of Cu, Ag, Au, Pt, and Hg Complexes. *Chem. Phys. Lett.* **2017**, *681*, 56–63.

93. Yannacone, S.; Oliveira, V.; Verma, N.; Kraka, E. A Continuum from Halogen Bonds to Covalent Bonds: Where Do λ^3 Iodanes Fit? *Inorganics* **2019**, *7*, 47.

94. Oliveira, V. P.; Marcial, B. L.; Machado, F. B. C.; Kraka, E. Metal-Halogen Bonding Seen through the Eyes of Vibrational Spectroscopy. *Materials* **2020**, *13*, 55.

95. Oliveira, V.; Cremer, D.; Kraka, E. The Many Facets of Chalcogen Bonding: Described by Vibrational Spectroscopy. *J. Phys. Chem. A* **2017**, *121*, 6845–6862.

96. Oliveira, V.; Kraka, E. Systematic Coupled Cluster Study of Noncovalent Interactions Involving Halogens, Chalcogens, and Pnicogens. *J. Phys. Chem. A* **2017**, *121*, 9544–9556.

97. Setiawan, D.; Kraka, E.; Cremer, D. Hidden Bond Anomalies: The Peculiar Case of the Fluorinated Amine Chalcogenides. *J. Phys. Chem. A* **2015**, *119*, 9541–9556.

98. Setiawan, D.; Kraka, E.; Cremer, D. Strength of the Pnicogen Bond in Complexes Involving Group VA Elements N, P, and As. *J. Phys. Chem. A* **2014**, *119*, 1642–1656.

99. Setiawan, D.; Kraka, E.; Cremer, D. Description of Pnicogen Bonding with the help of Vibrational Spectroscopy-The Missing Link Between Theory and Experiment. *Chem. Phys. Lett.* **2014**, *614*, 136–142.

100. Setiawan, D.; Cremer, D. Super-Pnicogen Bonding in the Radical Anion of the Fluorophosphine Dimer. *Chem. Phys. Lett.* **2016**, *662*, 182–187.

101. Sethio, D.; Oliveira, V.; Kraka, E. Quantitative Assessment of Tetrel Bonding Utilizing Vibrational Spectroscopy. *Molecules* **2018**, *23*, 2763–1–2763–21.

102. Freindorf, M.; Kraka, E.; Cremer, D. A Comprehensive Analysis of Hydrogen Bond Interactions Based on Local Vibrational Modes. *Int. J. Quantum Chem.* **2012**, *112*, 3174–3187.

103. Kalescky, R.; Zou, W.; Kraka, E.; Cremer, D. Local Vibrational Modes of the Water Dimer — Comparison of Theory and Experiment. *Chem. Phys. Lett.* **2012**, *554*, 243–247.

104. Kalescky, R.; Kraka, E.; Cremer, D. Local Vibrational Modes of the Formic Acid Dimer — The Strength of the Double H-Bond. *Mol. Phys.* **2013**, *111*, 1497–1510.

105. Tao, Y.; Zou, W.; Jia, J.; Li, W.; Cremer, D. Different Ways of Hydrogen Bonding in Water – Why Does Warm Water Freeze Faster than Cold Water? *J. Chem. Theory Comput.* **2017**, *13*, 55–76.

106. Tao, Y.; Zou, W.; Kraka, E. Strengthening of Hydrogen Bonding With the Push-Pull Effect. *Chem. Phys. Lett.* **2017**, *685*, 251–258.

107. Makoś, M. Z.; Freindorf, M.; Sethio, D.; Kraka, E. New Insights into Fe–H_2 and Fe–H^- Bonding of a [NiFe] Hydrogenase Mimic — A Local Vibrational Mode Study. *Theor. Chem. Acc.* **2019**, *138*, 76.

108. Lyu, S.; Beiranvand, N.; Freindorf, M.; Kraka, E. Interplay of Ring Puckering and Hydrogen Bonding in Deoxyribonucleosides. *J. Phys. Chem. A* **2019**, *123*, 7087–7103.

109. Verma, N.; Tao, Y.; Kraka, E. Systematic Detection and Characterization of Hydrogen Bonding in Proteins via Local Vibrational Modes. *J. Phys. Chem. B* **2021**, *125*, 2551–2565.

110. Beiranvand, N.; Freindorf, M.; Kraka, E. Hydrogen Bonding in Natural and Unnatural Base Pairs – Explored with Vibrational Spectroscopy. *Molecules* **2021**, *26*, 2268–1–2268–22.

111. Yannacone, S.; Freindorf, M.; Tao, Y.; Zou, W.; Kraka, E. Local Vibrational Mode Analysis of π-Hole Interactions between Aryl Donors and Small Molecule Acceptors. *Crystals* **2020**, *10*, 556–1–556–25.

112. Bader, R. F. W. *Atoms in Molecules: A Quantum Theory*, International Series of Monographs on Chemistry, Clarendon Press, Oxford, England, 1994.

113. Bader, R. F. W. A Quantum Theory of Molecular Structure and its Applications. *Chem. Rev.* **1991**, *91*, 893–928.

114. Bader, R. F. W. The Quantum Mechanical Basis of Conceptual Chemistry. *Monatsh. Chem.* **2005**, *136*, 819–854.

115. Popelier, P. L. *Atoms in Molecules: An Introduction*, Prentice Hall, New York, NY, 2000.

116. Fukui, K. The Path of Chemical Reactions — the IRC Approach. *Acc. Chem. Res.* **1981**, *14*, 363–368.

117. Hratchian, H. P.; Kraka, E. Improved Predictor-Corrector Integrators for Evaluating Reaction Path Curvature. *J. Chem. Theory Comput.* **2013**, *9*, 1481–1488.

118. Becke, A. D. Density-Functional Thermochemistry. III. The Role of Exact Exchange. *J. Chem. Phys.* **1993**, *98*, 5648–5652.

119. Lee, C.; Yang, W.; Parr, R. Development of the Colle-Salvetti Correlation-Energy Formula into a Functional of the Electron Density. *Phys. Rev. B* **1988**, *37*, 785–789.

120. Vosko, S.; Wilk, L.; Nusair, M. Accurate Spin-dependent Electron Liquid Correlation Energies for Local Spin Density Calculations: A Critical Analysis. *Can. J. Phys.* **1980**, *58*, 1200–1211.

121. Stephens, P.; Devlin, F.; Chabalowski, C.; Frisch, M. Ab Initio Calculation of Vibrational Absorption and Circular Dichroism Spectra Using Density Functional Force Fields. *J. Phys. Chem.* **1994**, *98*, 11623–11627.

122. Ditchfield, R.; Hehre, W. J.; Pople, J. A. Self-Consistent Molecular-Orbital Methods. IX. An Extended Gaussian-Type Basis for Molecular-Orbital Studies of Organic Molecules. *J. Chem. Phys.* **1971**, *54*, 724–728.

123. Hariharan, P. C.; Pople, J. A. The Effect of d-Functions on Molecular Orbital Energies for Hydrocarbons. *Chem. Phys. Lett.* **1972**, *16*, 217–219.

124. Cossi, M.; Barone, V.; Cammi, R.; Tomasi, J. *Ab Initio* Study of Solvated Molecules: A New Implementation of the Polarizable Continuum Model. *Chem. Phys. Lett.* **1996**, *255*, 327–335.

125. Tomasi, J.; Mennucci, B.; Cammi, R. Quantum Mechanical Continuum Solvation Models. *Chem. Rev.* **2005**, *105*, 2999–3093.

126. Byun, M.; Kim, M.-S.; Oh, B.-H. Crystal Structure of 5-3-Ketosteroid Isomerase Mutant D38N from

Pseudomonas Testosteroni Complexed with 5-α-Estran-3,17-Dione. doi:10.2210/pdb1OHP/pdb, 2003.

127. Case, D. A. *et al.*, AMBER, University of California, San Francisco, 2018.

128. Chung, L. W.; Sameera, W. M. C.; Ramozzi, R.; Page, A. J.; Hatanaka, M.; Petrova, G. P.; Harris, T. V.; Li, X.; Ke, Z.; Liu, F.; Li, H.-B.; Ding, L.; Morokuma, K. The ONIOM Method and its Applications. *Chem. Rev.* **2015**, *115*, 5678–5796.

129. Cremer, D.; Kraka, E. Chemical Bonds without Bonding Electron Density? Does the Difference Electron-Density Analysis Suffice for a Description of the Chemical Bond? *Angew. Chem. Int. Ed.* **1984**, *23*, 627–628.

130. Cremer, D.; Kraka, E. A Description of the Chemical Bond in Terms of Local Properties of Electron Density and Energy. *Croat. Chem. Acta* **1984**, *57*, 1259–1281.

131. Frisch, M. J. *et al.*, Gaussian, Wallingford CT, 2009.

132. Tao, Y.; Zou, W.; Freindorf, M.; Cremer, D.; Kraka, E. pURVA. Computational and Theoretical Chemistry Group (CATCO), Southern Methodist University, Dallas TX, 2021.

133. Dimitry Izotov, W. Z.; Cremer, D.; Kraka, E. Local Vibrational Mode Analysis, RING. Computational and Theoretical Chemistry Group (CATCO), Southern Methodist University, Dallas TX, 2021.

134. Zou, W.; Tao, Y.; Freindorf, M.; Makoś, M. Z.; Verma, N.; Cremer, D.; Kraka, E. Local Vibrational Mode Analysis LModeA, Computational and Theoretical Chemistry Group (CATCO), Southern Methodist University, Dallas TX, 2021.

135. Glendening, E. D.; Badenhoop, J. K.; Reed, A. E.; Carpenter, J. E.; Bohmann, J. A.; Morales, C. M.; Landis, C. R.; Weinhold, F. NBO6. Theoretical Chemistry Institute, University of Wisconsin, Madison (2013).

136. Keith, T. A. AIMALL. TK Gristmill Software: Overland Park KS, 2017.

137. Houck, W. J.; Pollack, R. M. Temperature Effects on the Catalytic Activity of the D38E Mutant of 3-Oxo-Δ^5-Steroid Isomerase: Favorable Enthalpies and Entropies of Activation Relative to the Nonenzymatic Reaction Catalyzed by Acetate Ion. *J. Am. Chem. Soc.* **2004**, *126*, 16416–16425.

138. Cremer, D.; Szabo, K. J. Ab initio Studies of Six-Membered Rings, Present Status and Future Developments, in *Conformational Behavior of Six-Membered Rings*, Juaristi, E., ed., Wiley-VCH, Weinheim, 1995, pp. 59–135.

139. Cremer, D. Calculation of Puckered Rings with Analytical Gradients. *J. Phys. Chem.* **1990**, *94*, 5502–5509.

140. Essén, H.; Cremer, D. On the Relationship Between the Mean Plane and the Least-Squares Plane of an N-Membered Puckered Ring. *Acta Crystallogr. B* **1984**, *40*, 418–420.

141. Cremer, D.; Kraka, E. Verification and Quantification of the Hammond–Leffler Postulate. *Rev. Processos Quim.* **2012**, *2012*, 27–30.

142. Kraka, E.; Cremer, D. Weaker Bonds with Shorter Bond Lengths. *Rev. Processos Quim.* **2012**, *2012*, 39–42.